

Metabolic regulatory network kinetic modeling with multiple isotopic tracers for iPSCs

Keqi Wang¹ | Wei Xie¹  | Sarah W. Harcum² 

¹Department of Mechanical and Industrial Engineering, Northeastern University, Boston, Massachusetts, USA

²Department of Bioengineering, Clemson University, Clemson, South Carolina, USA

Correspondence

Wei Xie, Department of Mechanical and Industrial Engineering, Northeastern University, Boston, MA 02115, USA.
 Email: w.xie@northeastern.edu

Sarah W. Harcum, Department of Bioengineering, Clemson University, Clemson, SC, USA.
 Email: harcum@clemson.edu

Funding information

National Institute of Standards and Technology, Grant/Award Numbers: 70NANB17H002, 70NANB21H086; National Science Foundation, Grant/Award Numbers: OIA-1736123, EEC-2100442

Abstract

The rapidly expanding market for regenerative medicines and cell therapies highlights the need to advance the understanding of cellular metabolisms and improve the prediction of cultivation production process for human induced pluripotent stem cells (iPSCs). In this paper, a metabolic kinetic model was developed to characterize the underlying mechanisms of iPSC culture process, which can predict cell response to environmental perturbation and support process control. This model focuses on the central carbon metabolic network, including glycolysis, pentose phosphate pathway, tricarboxylic acid cycle, and amino acid metabolism, which plays a crucial role to support iPSC proliferation. Heterogeneous measures of extracellular metabolites and multiple isotopic tracers collected under multiple conditions were used to learn metabolic regulatory mechanisms. Systematic cross-validation confirmed the model's performance in terms of providing reliable predictions on cellular metabolism and culture process dynamics under various culture conditions. Thus, the developed mechanistic kinetic model can support process control strategies to strategically select optimal cell culture conditions at different times, ensure cell product functionality, and facilitate large-scale manufacturing of regenerative medicines and cell therapies.

KEYWORDS

cell therapy manufacturing, induced pluripotent stem cells (iPSCs), metabolic regulatory network, process dynamic model, stable isotope labeling

1 | INTRODUCTION

Cell therapeutics and regenerative medicines have the potential to treat and prevent diseases, such as cancers, and cardiovascular and hematologic diseases (Hanna et al., 2016; Stephanopoulos et al., 1998). The cell therapy market is experiencing unparalleled growth and the projected worth of the relevant market is expected to be over \$8 billion in 2025 (Fiorenza et al., 2020). To meet the rising demand, cost reductions in manufacturing and increases in quality for

human induced pluripotent stem cells (iPSCs) on a large scale are crucial for the success of cell therapies (Odenwelder et al., 2021). Unlike traditional biopharmaceuticals, the cells are the product with functional identity depending on the regulatory metabolic dynamic behaviors.

The efficacy of the cells is very sensitive to culture conditions. Variability in the culture conditions can lead to reduced yields and heterogeneous cell populations. Heterogeneous cell populations have been observed to increase the potential for tumor or teratoma

This is an open access article under the terms of the [Creative Commons Attribution](https://creativecommons.org/licenses/by/4.0/) License, which permits use, distribution and reproduction in any medium, provided the original work is properly cited.

© 2023 The Authors. *Biotechnology and Bioengineering* published by Wiley Periodicals LLC.

formulation in the patient (Dressel, 2011). Traditional cell culture process control strategies often are ad hoc and rely solely on experimental approaches or PID controllers ignoring long-term effects. The optimal design and control of mammalian cell culture processes, especially iPSCs, can be laborious due to the limited understanding of cellular metabolisms and end-to-end cultivation process dynamics (Kyriakopoulos et al., 2018; Wang et al., 2021).

To determine the best culture conditions, accounting for cell life cycle, relationships between culture conditions and the output trajectory (i.e., cell functional identity and yield) are needed. Mechanistic dynamics model has the capability to predict cell outcomes (e.g., metabolic flux rates) and can be used to assess product quality and strategically select the optimal culture conditions at different times.

The proposed mechanistic model describes an iPSC metabolic network regulatory mechanisms. It is associated with the existing studies, including (1) metabolic flux analysis (MFA) (Niklas & Heinzle, 2012; Nolan & Lee, 2011), (2) ^{13}C -MFA (Antoniewicz, 2015, 2018; Dong et al., 2019; Leighty & Antoniewicz, 2011; Quek et al., 2010; Rivera-Ordaz et al., 2021; Sengupta et al., 2011; Wiechert et al., 2001), and (3) kinetic models (Ghorbaniaghdam et al., 2014, 2013, 2014; Kyriakopoulos et al., 2018; Nolan & Lee, 2011). In MFA, metabolic flux rates (such as substrate uptake rate and metabolite secretion rate) are estimated based on experimental measurements subject to stoichiometric constraints. Under the standard assumption of (pseudo) steady state for intracellular metabolites, the sum of all fluxes producing a metabolite is equal to the sum of all fluxes consuming that metabolite. This technique is frequently used to compare the metabolism of different cell lines to assess the activity of individual pathways under different cultivation conditions (Niklas & Heinzle, 2012). However, intracellular metabolites can change during cell proliferation (Templeton et al., 2013).

Stable isotope studies, integrating with MFA, have provided more detailed information on intracellular state and metabolic pathways, namely ^{13}C -MFA can precisely estimate metabolic reaction rates. Typically these flux rates are estimated from measured intracellular mass isotopomer distribution (MID) patterns and external metabolites concentrations. Common ^{13}C and ^2H isotopic tracers were utilized for investigating mammalian cell metabolism with a specific emphasis on the interpretation of isotopic labeling patterns (Dong et al., 2019). Many existing studies are built on the assumption of isotopic and metabolic steady state (Antoniewicz, 2015, 2018; Dong et al., 2019; Quek et al., 2010; Rivera-Ordaz et al., 2021; Sengupta et al., 2011; Wiechert et al., 2001). Several modeling tools have been developed for situations involving isotopic and/or metabolic non-steady states (Antoniewicz, 2015, 2018; Leighty & Antoniewicz, 2011).

Another approach to model cell dynamics includes kinetic-metabolic models (Kyriakopoulos et al., 2018). The vast majority of the kinetic models use Monod and Michaelis-Menten (MM) expression formalisms modeling the metabolic regulation mechanisms (Ghorbaniaghdam et al., 2014, 2013, 2014; Kyriakopoulos et al., 2018; Nolan & Lee, 2011). For Chinese hamster ovary (CHO) cell cultures,

kinetic-metabolic models include glycolysis, pentose phosphate pathway (PPP), tricarboxylic acid (TCA) cycle, respiratory chain, as well as the regulatory functions from energy shuttles (ATP/ADP) and cofactors (NADH, NAD^+ , NADPH, NADP^+); this high level of details is required to predict hypoxic perturbation (Ghorbaniaghdam et al., 2013, 2014). For example, the study (Nolan & Lee, 2011) proposed a Monod model characterizing the cell flux rate response to environmental perturbation. That study used limiting substrate kinetics to calculate the extracellular metabolite consumption/production rates and further infer metabolic flux rates built on a static MFA assumption, that is, assuming the intracellular metabolites are at the pseudo-steady state. Even though several *in silico* metabolomic platforms have been developed for CHO cells (Ghorbaniaghdam et al., 2014, 2013, 2014; Kyriakopoulos et al., 2018; Nolan & Lee, 2011), a metabolic regulatory network simulator for iPSC has not been developed.

As lactate accumulation emerges as an inevitable outcome of iPSC metabolism, it becomes essential to explore the consequences of accumulated extracellular lactate on intracellular iPSC metabolism. Equally important is to comprehend how glucose concentration acts as a regulatory factor, influencing lactate production. Understanding the implications of these concentration variations is not only critical for the survival and proliferation of iPSCs (Nelson et al., 2008) but also essential for maintaining the quality of cell products. Hence, the main objective of this study is to develop and validate a mechanistic model of an iPSC metabolic regulatory network that can precisely predict cell responses to environmental changes, with a particular focus on variations in extracellular glucose and lactate concentrations.

The proposed model primarily focuses on central metabolism, given its pivotal role in stem cell proliferation, biosynthesis, and overall functionality. To estimate model parameters, this model utilized experimentally obtained data from well-designed monolayer K3 iPSC cultures, as described in the study (Odenwelder et al., 2021). During the model development, the level of detail required for key pathways was explored, namely the PPP and branched amino acids uptake rates into the TCA cycle. In this paper, the proposed kinetic model structure with critical regulatory mechanisms will be discussed and validated through comparisons with the experimental data, with the aim of ensuring the model's ability to accurately predict cell responses to environmental changes.

The proposed mechanistic model, comprising the metabolic reaction network structure and flux regulatory mechanism, can be easily customized to suit various mammalian cell culture systems, for example, embryonic stem cells (ESCs), CHO, etc. This adaptability arises from the underlying principles and general characteristics of metabolic regulation that are common across various mammalian cells. Through the collection of extracellular metabolite concentrations and intracellular MID measurements, this mechanistic model can be adeptly employed to analyze and forecast the behavior of other mammalian cell cultures with consistent accuracy and reliability.

TABLE 1 The media formulations for K3 iPSC cultures include initial concentrations of glucose, sodium L-lactate, and supplemented sodium chloride (NaCl).

Component	Concentrations (mM)			
	HGLL	HGHL	LGLL	LGHL
Glucose	18.3	18.3	5.6	5.6
Lactate	-	20.0	-	20.0
Added NaCl	+20.0	-	+20.0	-

Note: NaCl was added to balance osmolarity in cultures lacking sodium lactate. Additionally, the media contains 2.75 mM L-glutamine.

Abbreviations: HGHL, high glucose and high lactate; HGLL, high glucose and low lactate; LGHL, low glucose and high lactate; LGLL, low glucose and low lactate.

2 | DATA DESCRIPTION

Briefly, the data used to estimate the model parameters were derived from an experimental study of K3 iPSCs, where monolayer cultures were conducted in 6-well plates and 60 mm cell culture dishes (Odenwelder et al., 2021). The data encompassed extracellular metabolite measurements and isotopic labeling details for four distinct culture conditions, utilizing three tracers: glucose, glutamine, and lactate. The four different initial culture media concentrations were: (1) high glucose and low lactate (HGLL); standard initial conditions, that is, 18.3 mM glucose and 0 mM lactate; (2) high glucose and high lactate (HGHL), that is, 18.3 mM glucose and 20 mM lactate; (3) low glucose and low lactate (LGLL), that is, 5.6 mM glucose and 0 mM lactate; and (4) low glucose and high lactate (LGHL), that is, 5.6 mM glucose and 20 mM lactate. Table 1 presents the media concentrations used for each condition, encompassing glucose, lactate, and supplemented sodium chloride concentrations. Furthermore, 2.75 mM glutamine was included in each condition. These concentrations were chosen to ensure comparable growth rates across all conditions while maintaining pluripotency (Odenwelder et al., 2021).

Cell density, glucose, lactate, pyruvate, and extracellular amino acid concentrations were obtained for each condition at 0-, 12-, 24-, 36-, and 48-h. Intracellular amino acid MIDs were obtained from parallel labeling experiments that used [1,2-¹³C₂] glucose, [U-¹³C₅] L-glutamine, and [U-¹³C₃] sodium L-lactate (when lactate was added to the culture media). The time-course measurements, as illustrated in Figure 1, included the transition to metabolic and isotopic steady states (Odenwelder et al., 2021). These measurements were used to develop the metabolic regulatory network kinetic model for iPSC cultures.

3 | MODEL DEVELOPMENT

iPSCs cultured in petri-dish 2D monolayer have homogeneous environmental condition. Thus, the objective of this study is to develop a deterministic metabolic regulatory network kinetic model

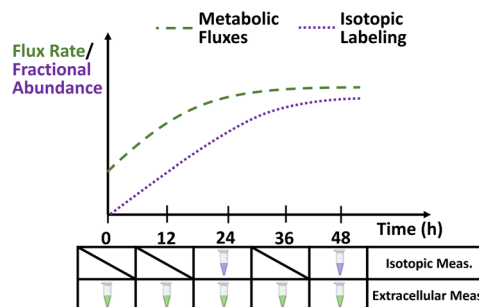


FIGURE 1 Schematic for cell metabolic and isotopic states when time-course measurements of extracellular concentrations and intracellular MIDs were taken during the experimental iPSC cultures (Adapted from Jazmin and Young (Jazmin & Young, 2013) and created with BioRender.com). Metabolic steady state is reached before isotopic steady state (Odenwelder et al., 2021). iPSC, induced pluripotent stem cells; MID, mass isotopomer distribution.

characterizing the mean metabolic dynamics, which is presented in four developmental stages. Section 3.1 provides the general dynamic model description, including (1) metabolic reaction network kinetic model; and (2) time-course isotopic labeling simulation. Section 3.2 presents the iPSC metabolic reaction network which includes central carbon metabolism. In Section 3.3, the metabolic flux kinetic model, characterizing cell response to environmental variations, is fitted by using time-course extracellular concentration measurements and MIDs. Finally, in Section 3.4, the assessment of fit and validation of the dynamic model for the iPSC cultures is discussed, where the objective function and goodness-of-fit will be presented.

3.1 | Metabolic network kinetic modeling

In this section, the general regulatory metabolic network kinetic model and time-course isotopic labeling simulation are presented. The kinetic model captures the dynamic changes in cell density, and extracellular and intracellular metabolite concentrations, where the changing rates of metabolites depend on the concentration of substrates and inhibitors. To incorporate the mass isotopic data, a dynamic isotopic labeling system was constructed, and a time-course isotopic labeling simulation was developed. Overall, the metabolic reaction network kinetic model provides a comprehensive understanding of the underlying mechanisms of the iPSC cultures.

(1) Metabolic Reaction Network Kinetic Model. The data from the study for K3 iPSCs were collected during the exponential growth phase (Odenwelder et al., 2021). Through experimental design and statistical analysis, our previous study (Odenwelder et al., 2021) discovered uniform specific cell growth rates (μ) across the four batch culture conditions (HGLL, HGHL, LGLL, and LGHL), maintaining pluripotency. This suggests that glucose and lactate concentrations within these ranges did not notably influence K3 iPSC growth rates and did not have a detrimental impact on human K3 iPSC pluripotency. Thus the classical cell density formalism was used to

relate growth and the cell density, denoted by $X(t)$ (cells/cm²), at time t as,

$$\frac{dX(t)}{dt} = \mu X(t). \quad (1)$$

The extracellular metabolite concentrations at time t are denoted by a vector with dimension p , that is, $s(t) = (s_1(t), s_2(t), \dots, s_p(t))^T$. Similarly, the intracellular metabolite concentrations of interest are denoted by a vector with dimension q at time t as $l(t) = (l_1(t), l_2(t), \dots, l_q(t))^T$. Thus, at any time t , the state of extracellular and intracellular metabolite concentrations is denoted by

$$u(t) = (s(t)^T, l(t)^T)^T.$$

To model the dynamic evolution of cell response to environmental fluctuations during the iPSC cultures, at any time t , the specific reaction flux rates, represented by a vector with dimension n , depend on both extracellular and intracellular metabolite concentrations, that is,

$$v[u(t)] = (v_1[u(t)], v_2[u(t)], \dots, v_n[u(t)])^T.$$

Let N denote a $(p+q) \times n$ stoichiometry matrix characterizing the structure of metabolic reaction network. Therefore, the dynamic evolution of extracellular and intracellular metabolite concentrations is modeled through a mass balance on the system of equations,

$$\frac{du(t)}{dt} = Nv[u(t)]X(t). \quad (2)$$

To capture the cell response to environmental perturbation, a MM formalism based regulation model was used to characterize the relationship of metabolic flux rates depending on the concentrations of associated substrates and inhibitors. This allows leveraging the existing biology knowledge and facilitating the learning of regulation mechanisms of iPSC metabolic reaction network from the experimental data.

Specifically, the g -th flux rate at the time t is modeled as,

$$v_g[u(t)] = v_{max,g} \prod_{y \in \Omega_y^g} \frac{u_y(t)}{u_y(t) + K_{m,y}} \prod_{z \in \Omega_z^g} \frac{K_{i,z}}{u_z(t) + K_{i,z}}, \quad (3)$$

for $g = 1, 2, \dots, n$, where the set Ω_y^g represents the collection of activators (such as nutrients and substrates) influencing the flux rate v_g and the set Ω_z^g represents the collection of inhibitors dampening v_g . The parameters $K_{i,\cdot}$, $K_{m,\cdot}$, and $v_{max,\cdot}$ represent the affinity constant, the inhibition constant, and the maximum specific flux rate respectively. For iPSC cultures, the experimental data referenced were used to identify the critical activators and inhibitors, as well as learning the MM regulation model coefficients.

(2) Time-Course Isotopic Labeling Simulation. Different ¹³C-labeling patterns are generated by different flux distributions $v[u(t)]$. Thus, incorporating the dynamic system of isotopic

labeling patterns (MID), which is a vector containing the fractional abundance of each mass state of metabolites, into the metabolic network kinetic model can aid in understanding intercellular metabolic network mechanisms. However, modeling each individual atom as one system state variable is computationally expensive. To address this issue, the elementary metabolite unit (EMU) framework was proposed, and it is based on a highly efficient decomposition method that can identify the minimum amount of information needed to simulate isotopic labeling (Antoniewicz et al., 2007). Basically, the EMUs are created by using a decomposition algorithm and form the new basis for generating system equations that describe the relationship between fluxes and isotope measurements; see more detailed information in studies (Ahn & Antoniewicz, 2011, 2013; Antoniewicz, 2015, 2018, 2021; Antoniewicz et al., 2007; Jazmin & Young, 2013).

Based on the study (Antoniewicz et al., 2007; Young et al., 2008), the reduced system can be obtained after decoupling based on EMUs with size $r = 1, 2, \dots, R$ and connectivity. The time-dependent network was first identified: the decoupled EMUs with size r network, $G_r(t) = \{V_r, E_r, W_r(t)\}$ with $r = 1, 2, \dots, R$. The vector $V_r = (V_r^{(a)T}, V_r^{(b)T})^T$ is the set of vertices (i.e., EMUs) within the r -th network, the vector $V_r^{(b)}$ with dimension $|V_r^{(b)}|$ is the set of input EMUs (i.e., EMUs with size smaller than r or EMUs of extracellular carbon sources), the vector $V_r^{(a)}$ with dimension $|V_r^{(a)}|$ is the set of EMUs with size r . E_r is the adjacency matrix with dimension $(|V_r^{(a)}| + |V_r^{(b)}|) \times (|V_r^{(a)}| + |V_r^{(b)}|)$ representing the dependence between each vertex. The corresponding weight matrix $W_r(t)$ varies with time t . The non-negative (i, j) -th element $W_r^{(i,j)}(t)$ indicates the flux rate of the reaction producing i -th EMU by consuming j -th EMU at time t .

Thus, at any time t , the dynamic isotopic labeling system can be defined as:

$$\frac{dC_r(t)}{dt} = \frac{A_r(t) \cdot C_r(t) + B_r(t) \cdot D_r(t)}{P_r(t)}, \quad (4)$$

where the rows of the state matrix $C_r(t)$ correspond to the MIDs of EMUs within $V_r^{(a)}$ at time t . The input matrix $D_r(t)$ is analogous but with rows of input/carbon sources EMUs within $V_r^{(b)}$ at time t . The concentration matrix $P_r(t)$ is a diagonal matrix whose elements are pool sizes corresponding to EMUs represented in $V_r^{(a)}$. The construction of $A_r(t)$ and $B_r(t)$ are based on the decoupled EMU reaction network $G_r(t)$. The system matrix $A_r(t)$ with size $|V_r^{(a)}| \times |V_r^{(a)}|$ and matrix $B_r(t)$ with size $|V_r^{(a)}| \times |V_r^{(b)}|$ describe the metabolic network with elements defined as follows:

$$A_r^{(i,j)}(t) = \begin{cases} -\sum_{k=1}^{|V_r^{(a)}|} W_r^{(k,j)}(t), & i = j, \\ W_r^{(i,j)}(t), & i \neq j; \end{cases} \quad (5)$$

and

$$B_r^{(i,j)}(t) = W_r^{(i,|V_r^{(a)}|+j)}(t). \quad (6)$$

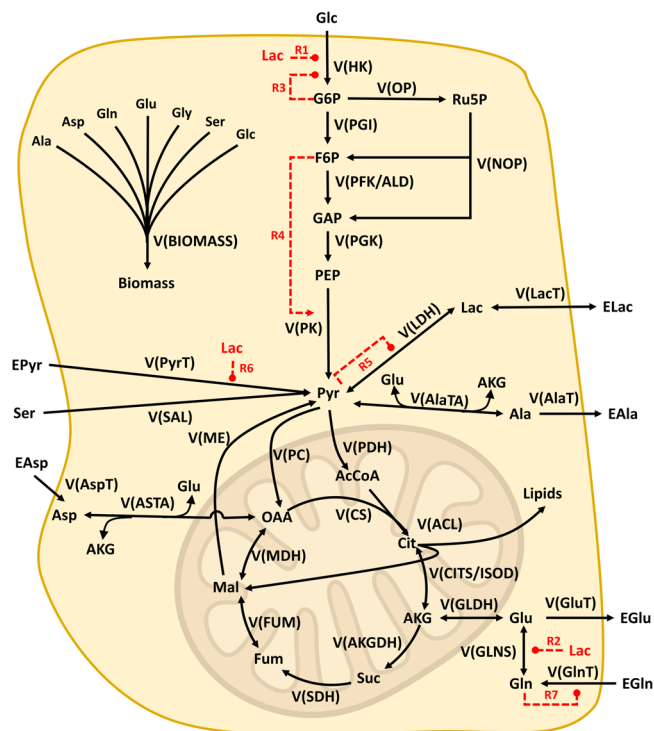


FIGURE 2 An illustration of the iPSC regulatory metabolic network (Created with BioRender.com). Glycolysis, PPP, TCA and anaplerosis and amino acid utilization are shown. Additionally, the regulatory mechanisms included in the dynamic model are shown. The metabolites descriptions are listed in Table A3. The enzyme description, including the Enzyme Commission Numbers (EC-No.) for each reaction, is listed in Table A4. iPSC, induced pluripotent stem cells; PPP, pentose phosphate pathway; TCA, tricarboxylic acid.

3.2 | iPSC metabolic reaction network

The developed iPSC metabolic network model leverages central carbon metabolism from several previously published metabolic frameworks (Dressel, 2011; Fiorenza et al., 2020; Ghorbaniaghdam et al., 2013, 2014; Niklas & Heinze, 2012; Odenwelder et al., 2021) and further learns from data. The iPSC metabolic network included glycolysis, TCA cycle, anaplerosis, PPP, and amino acid metabolism. For simplification, the reactions of PPP were collapsed into two reactions: Oxidative phase/branch and Non-oxidative phase/branch (i.e., No. 9 & 10 reaction in Table A1). During the exponential phase, greater than 90% of pentose-phosphate carbons is returned to glycolysis for the mammalian cell (Halestrap, 2012; Templeton et al., 2013). Thus, the synthesis of nucleotides and nucleic acids is considered as an insignificant contributor to the model. The metabolic network is shown in Figure 2 and the metabolic stoichiometry is listed in Table A1. The descriptions of metabolites and the enzymes conform to the Enzyme Commission Number (EC-No.) and are provided in Tables A3 and A4, respectively.

While this model primarily focuses on central carbon metabolism, it's worth noting that the additional model's structure,

including metabolic reaction pathways (e.g., one-carbon metabolism, fatty acid oxidation, and nucleotide biosynthesis) and the associated flux regulatory mechanisms, could be easily incorporated.

3.3 | Biokinetic model of flux regulatory mechanism

Due to the lack of energetic state and redox level measurements, each metabolic flux rate is modeled as dependent on the substrates and inhibitors concentrations using MM model formalism. Similar to the existing studies (Dressel, 2011; Fiorenza et al., 2020; Ghorbaniaghdam et al., 2014), for simplification purposes and also due to a lack of available data in the literature, a single affinity constant value is used for each metabolite. Additionally, reaction reversibility was considered during the iPSC culture model development for some key reactions. The final model is fully described in Table A2. Several regulatory mechanisms (i.e., No. R1 to R7) are highlighted in Figure 2, which were incorporated into the metabolic flux kinetic model to improve the model's prediction capability and better characterize the responses to environmental variations. These key final reactions are described below, where these new dependencies are highlighted in under brackets ... with the corresponding regulatory mechanism No., while the original nomenclature is outside the brackets.

1. Lactate accumulation has previously been reported to reduce glycolytic activity by inhibiting hexokinase (HK) and phosphofruktokinase (PFK) activity in mammalian cells, where lactate acts as a signaling molecule to down-regulate PFK activity (CostaLeite et al., 2007; Ivarsson et al., 2015; Mulukutla et al., 2012). After evaluation of the experimental data, the model for HK was updated to include this inhibitory effect of lactate on it:

$$v(HK) = v_{max,HK} \times \frac{Glc}{K_{m,Glc} + Glc} \times \frac{K_{i,LactoHK}}{K_{i,LactoHK} + Lac} \quad (7)$$

2. Since lactate inhibits glutaminase activity—the enzyme responsible for converting glutamine (GLN) to glutamate (GLU) (Glacken et al., 1988; Hassell et al., 1991)—the forward (*f*) flux rate for the reaction, that is, $Gln \leftrightarrow Glu + NH_4$, was updated,

$$v(GLNSf) = v_{max,fGLNS} \times \frac{Gln}{K_m, Gln + Gln} \times \frac{K_{i,LactoGLNS}}{K_{i,LactoGLNS} + Lac} \quad (8)$$

3. Several regulatory functions, adapted from the studies (Ghorbaniaghdam et al., 2014, 2013, 2014), were evaluated using the experimental data to characterize activations and inhibitions.

The regulatory mechanisms involved in glycolysis are described as: (a) hexokinase inhibition by its product G6P, see **R3** in eq (9); (b) activation of pyruvate kinase by F6P, see **R4** in eq (10), as well as (c) the inhibition of lactate dehydrogenase reverse (*r*) reaction, see **R5** in eq (11), was changed to include the G6P inhibition:

$$v(HK) = v_{max,HK} \times \frac{Glc}{K_{m,Glc} + Glc} \times \frac{K_{i,LactoHK}}{K_{i,LactoHK} + Lac} \times \frac{K_{i,G6P}}{K_{i,G6P} + G6P}; \quad (9)$$

R3

$$v(PK) = v_{max,PK} \times \frac{PEP}{K_{m,PEP} \times \left[1 + \frac{K_{a,F6P}}{F6P} \right] + PEP}; \quad (10)$$

R4

$$v(LDHR) = v_{max,rLDH} \times \frac{Lac}{K_{m,Lac} + Lac} \times \frac{K_{i,Pyr}}{K_{i,Pyr} + Pyr}. \quad (11)$$

R5

4. Both lactate and pyruvate transport across the plasma membrane are facilitated by proton-linked monocarboxylate transporters (MCTs) (Halestrap, 2012; Huckabee, 1956). More favorable lactate transport kinetics may decrease pyruvate consumption under high lactate culture conditions (Draoui & Feron, 2011; Odenwelder et al., 2021). Thus, the model of PyrT was updated to:

$$v(PyrT) = v_{max,PyrT} \times \frac{EPyr}{K_{m,EPyr} + EPyr} \times \frac{K_{i,LactoPyr}}{K_{i,LactoPyr} + Lac}. \quad (12)$$

R6

5. Since the transportation of extracellular-glutamine via cell membrane can be inhibited by intracellular-glutamine, the model for GlnT was updated to:

$$v(GlnT) = v_{max,GlnT} \times \frac{EGln}{K_{m,EGln} + EGln} \times \frac{K_{i,GLN}}{K_{i,GLN} + GLN}. \quad (13)$$

R7

3.4 | Model fit and goodness-of-fit assessment

The proposed iPSC metabolic network kinetic model focuses on characterizing central carbon metabolism, including significant reactions from glycolysis, the TCA cycle, anaplerosis, PPP, and amino

acid metabolism, along with regulatory mechanisms, across distinct cultural environments characterized by varying levels of glucose and lactate concentrations. The final model developed is shown in Table A1. This model includes 30 metabolic reactions with 32 variables (metabolites' concentration) in the reaction equations. The iPSC metabolic flux rate regulation biokinetic model, presented in Table A2, incorporates key activators and inhibitors for each reaction, describing the regulatory effects through the MM model. The proposed iPSC culture kinetic model estimates model parameters using both extracellular and MID data collected over time under the four different culture conditions. The extracellular metabolite concentration measurements at time *t* are denoted as s_t^{meas} for *t* = 0, 12, 24, 36, 48 hours (h). To ensure the model's accuracy and minimize the impact of measurement errors, values that fell below the detection limit of the Cedex Bioanalyzer are treated as missing data. The intracellular isotopic labeling measurements at time *t'* are denoted as MID_t^{meas} for *t'* = 24 and 48 h. The MID measurements obtained from [U- $^{13}C_3$] lactate for the high glucose high lactate and low glucose high lactate cultures exhibited considerable measurement errors, as reported in the study (Odenwelder et al., 2021). Consequently, these measurements were intentionally excluded from the training data set used for developing the proposed model.

For model fitting, the objective is to minimize the weighted sum of squared residuals (SSR) between the available experimental data, which includes both extracellular metabolite concentrations (s_t^{meas}) and intracellular isotopic labeling (MID_t^{meas}), and the corresponding model-predicted values (s_t^{sim} and MID_t^{sim}),

$$\min SSR = \sum_{t=1}^T \frac{(s_t^{sim} - s_t^{meas})^2}{var_t^s} + \sum_{t'=1}^{T'} \frac{(MID_t^{sim} - MID_t^{meas})^2}{var_t^M}, \quad (14)$$

where the weights are the inverse of the variances of the experimental measurements on extracellular metabolites and MIDs, that is, (var_t^s , var_t^M). The fitting criteria in eq (14) allows the model to systematically and effectively fit the metabolic regulation network at different times.

The initial conditions for extracellular metabolites were obtained from culture data. As the experimental data only includes the relative abundance and the MIDs, estimates for the initial intracellular metabolite concentrations were sourced from the BRENDA Enzyme Database (Chang et al., 2021) and related references for mammalian cells cultured under similar conditions. Similarly, the initial kinetic parameter values were taken from the BRENDA Enzyme Database (Chang et al., 2021) and relevant references for similar metabolic networks and pathways.

The goodness-of-fit for the developed iPSC metabolic kinetic model was assessed based on predictions using a χ^2 test. Basically, the null hypothesis is that the fitted model can faithfully represent the iPSC culture metabolic mechanism. This test assumes that the minimized variance-weighted SSR follows a χ^2 distribution with *d* degrees of freedom, where the degree of freedom *d* equals the number of observations minus the number of fitted parameters. In

this study, the χ^2 statistical test has p -value much greater than 0.05 indicating the model predictions are not significantly different than the measured values.

4 | RESULTS AND DISCUSSION

The proposed mechanistic model was developed based on a small set of experimental data (see Section 2) and the model predictive performance was then validated in two manners. First, to mimic the dynamic data collection and assess the rolling forecasts required for process control, at any time t , historical data were used to fit the model up to t and then the fitted model was used to predict the remainder of the culture behavior. In Section 4.1, the model's ability to capture the dynamic evolution of iPSC metabolic characteristics was evaluated. The model was trained on experimental data collected over different time intervals (0–12-h, 0–24-h, and 0–36-h), and used to predict the iPSC culture for up to 48-h.

Second, to assess the model's ability to generalize and extrapolate to new culture conditions, three data sets, randomly selected from (1) HGLL; (2) HGHL; (3) LGLL; and (4) LGHL, were used to predict the fourth data set with different initial conditions in Section 4.2. Basically, three data sets were used to train the model, and then the model was used to predict the fourth data set behaviors. This training/test data set selection and evaluation strategy is built on the philosophy of cross validation that is often used in the literature on model selection (McLachlan, 2005; Refaeilzadeh et al., 2009). Each culture condition was examined in succession using the other three

data sets. Therefore, by validating the model's prediction performance under different experimental conditions, its robustness and usefulness for predicting iPSC characteristics in a variety of settings is verified.

4.1 | Prediction of iPSC culture process

During the model validation process, the proposed model simulator was trained using experimental data collected over various time intervals (0–12-h, 0–24-h, and 0–36-h). The model's ability to predict the dynamic trajectories of key metabolites, including glucose, lactate, glutamate, glutamine, and pyruvate, as well as cell density, was evaluated by comparing the predicted values to experimental observations up to 48 h. Figure 3 provides a representative result of the cell culture process prediction for the case starting with HGLL. The results for the remaining settings, including HGHL, LGLL, and LGHL, are presented in Appendix Figure B1–B3.

The χ^2 test was employed to assess the goodness-of-fit of the proposed mechanistic model trained using the historical data collected in different time intervals. The statistical test for the model trained on 0–12-h of experimental data yielded a value of 33.6 with 47 degrees of freedom ($p = 0.93$). Similarly, for the model trained on 0–23-h and 0–36-h of experimental data, the test statistics was 82.6 with 107 degrees of freedom ($p = 0.96$) and 138.1 with 167 degrees of freedom ($p = 0.95$), respectively. All of the p exceed 0.05, suggesting that the proposed metabolic kinetics

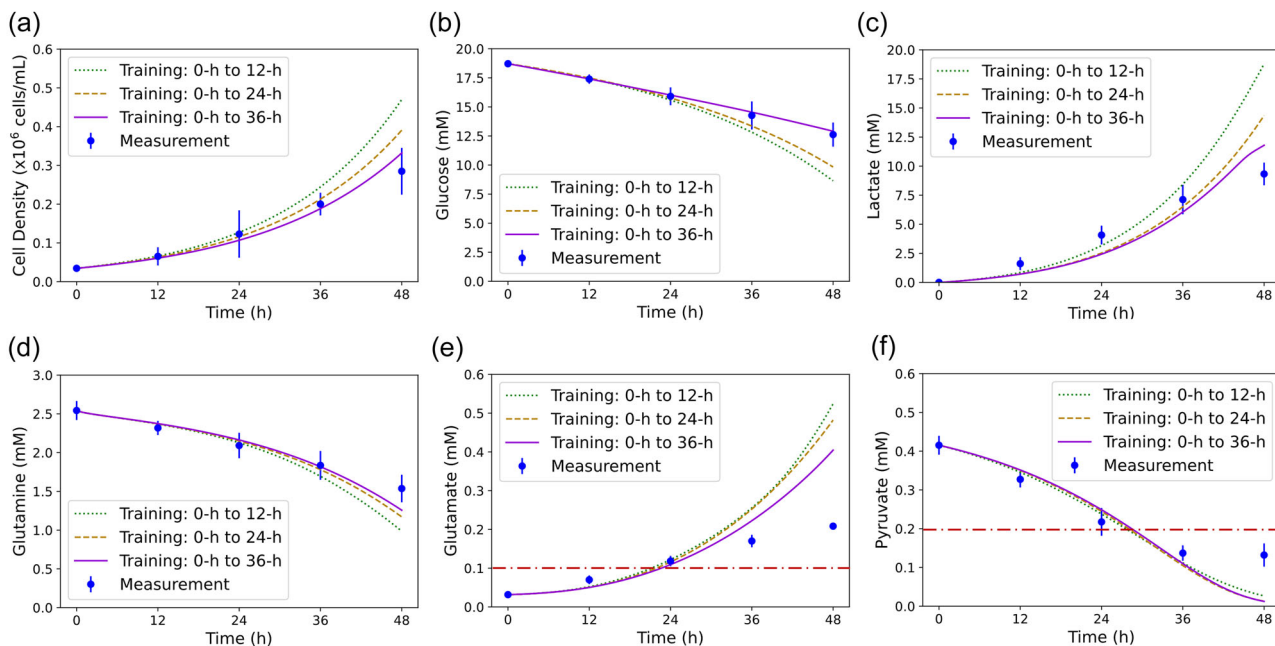


FIGURE 3 Dynamic model trained with historical data collected under different time intervals—Cell characteristic predictions for high glucose and low lactate cultures. (a) Cell density, (b) Glucose, (c) Lactate, (d) Glutamine, (e) Glutamate, and (f) Pyruvate. Times 0–12-h (green dotted line); Times 0–24-h (brown dashed line); and Times 0–36-h (purple solid line). The detection limit of the Cedex Bioanalyzer is shown as the red dash-dot line.

model fits well with the experimental data set. The results in Figure 3 demonstrate that the fitted model can provide improved predictions for most of the metabolite trajectories as more data are collected over time.

Overall, the predicted profiles of the iPSC cultures can closely track the dynamic patterns of the measured profiles and capture the cell culture dynamics. The experimental iPSC data were obtained from plates and dishes with limited space. Even though the overall growth rates were the same across the four conditions by experimental design, the growth rate decreased with time as nutrients were consumed and metabolic wastes accumulated. It is important to note that the developed mechanistic metabolic kinetic model is a simplified representation of the iPSC central carbon metabolic network, there could likely be some key metabolic regulations and biochemical reactions that were not incorporated. The less accurate predictive performances for lactate (under low lactate conditions) and glutamate may be due to the omission of key reactions or regulatory functions. For example, as suggested by the calibrated model in previous studies (Ghorbaniaghdam et al., 2014, 2013, 2014), the membrane transportation of glutamate for mammalian cells is significantly impacted by the energetic state (ATP and ADP), and the forward and reverse conversion of lactate to pyruvate is influenced by the redox level (NAD and NADH).

Since the redox level and energetic state-related measurements were not collected for the iPSC cultures, these factors were not accounted for in the current model. The study (Nolan & Lee, 2011) found for CHO cells, a redox parameter assisted with lactate predictions; however, the redox parameter implemented by this

study was unmeasurable and thus would be difficult to incorporate into a control model. Furthermore, the lower prediction performance for glutamate may be attributed to its involvement in multiple reactions (see Figure 2), leading to error accumulation over time. Future work should address these limitations with more comprehensive experimental data for iPSC cultures.

4.2 | Prediction across different initial conditions

To assess the predictive capability of the proposed mechanistic model across various initial culture conditions and enhance the understanding of iPSCs response to environmental changes, specifically glucose and lactate, a cross-validation approach was employed. This approach first trained the model with three of the four data sets (i.e., HGLL, HGHL, LGLL, and HGHL). The remaining data set behavior was then predicted. This approach provided valuable insight for optimizing Design of Experiments strategies in the realm of *in silico* experimentation.

The model cross-validation prediction for the HGLL culture was evaluated using the model trained on HGHL, LGLL, and LGHL data sets, as illustrated in Figure 4. The other three across-validation predictions are provided in Appendix Figure C1–C3. Cell density and key metabolites (i.e., glucose, lactate, glutamate, glutamine, and pyruvate) were predicted and are shown with the average of the measured values with standard deviations. To evaluate the goodness-of-fit, the χ^2 test SSR statistics is 783 with 802 degrees of freedom with $p = 0.67$ much greater than 0.05. This p-value indicates that the metabolic kinetic model can faithfully represent the iPSC culture

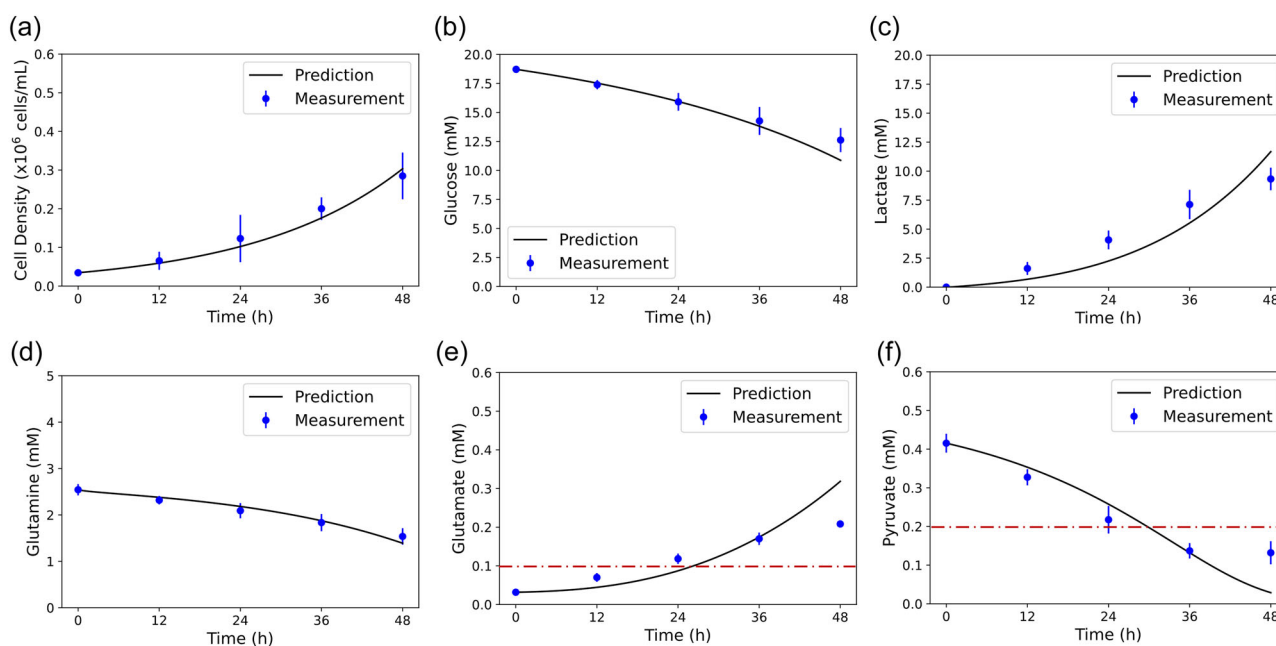


FIGURE 4 Dynamic model trained with three other data sets with varied initial glucose and lactate concentrations for cell characteristic predictions in high glucose and low lactate cultures. (a) Cell density, (b) Glucose, (c) Lactate, (d) Glutamine, (e) Glutamate, and (f) Pyruvate. The detection limit of the Cedex Bioanalyzer is shown as the red dash-dot line.

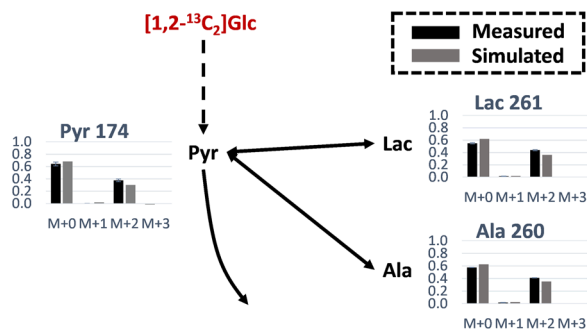


FIGURE 5 MID measurements and predictions for the [1,2-¹³C₂] glucose tracer at 48-h for high glucose low lactate cultures using the dynamic model trained on the other three data sets compared to literature measurements. MID, mass isotopomer distribution.

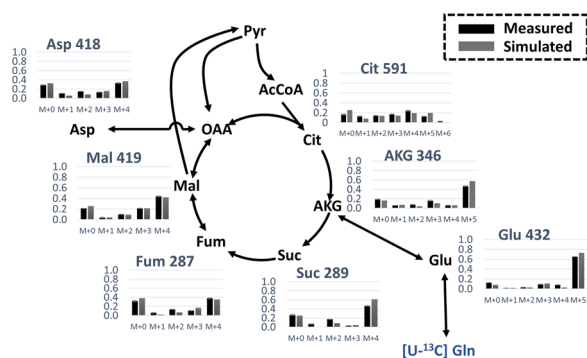


FIGURE 6 MID measurements and predictions for the [U-¹³C₅] glutamine tracer at 48-h for high glucose low lactate cultures using the dynamic model trained on the other three data sets compared to literature measurements. MID, mass isotopomer distribution.

regulatory mechanisms under different levels of glucose and lactate concentrations.

The predictions of intracellular MID from the [1,2-¹³C₂] glucose and [U-¹³C₅] glutamine tracer at 48-h under the control (HGLL) culture condition are shown in Figure 5 and 6, respectively. Even though there is some prediction error, the simulation model can correctly predict the dynamics and interdependencies of multivariate iPSC culture process metabolism. The developed metabolic kinetic model can faithfully predict the cell response to environmental perturbation, which could guide the strategic feeding strategy for the integrated iPSC culture process for future research. In addition, by incorporating even the simplified PPP reactions, the M+1 isotopic labeling pattern for pyruvate and related metabolites from [1,2-¹³C₂] glucose tracer can be well-predicted.

The prediction of metabolic flux maps for K3 iPSC under control culture at 24-h and 48-h are shown in Figure 7. The prediction performance of metabolic concentration trajectory and flux maps for K3 iPSC under HGHL, LGLL, and LGHL are provided in Appendix Figure D1–D3. Since no restrictive steady-state assumption was required for the developed metabolic kinetic

model, the flow-in flux is not required to be equal to the flow-out flux for each metabolite.

The prediction of metabolic flux dynamics for K3 iPSC culture reveals several significant observations. First, the glycolytic efficiency, which measures how effectively K3 iPSCs utilize glucose as an energy source, remained consistently high across all conditions, exceeding 1.6 and approaching the theoretical maximum of 2.0 moles of lactate produced per mole of glucose consumed. This suggests that K3 iPSCs are efficiently converting glucose into lactate with minimal byproduct production. Second, the [U-¹³C₃] lactate tracer showed that K3 iPSCs consumed and metabolized lactate in the high lactate cultures. However, in all four culture conditions, there was a net production of lactate, indicating that K3 iPSCs produced and also consumed lactate in the high lactate culture conditions. Third, in the control experimental setting, as the iPSC cultures approached the late exponential phase, there was a gradual increase in the flux rates of the TCA cycle, consistent with findings reported in a previous literature study (Templeton et al., 2013). Finally, the mechanistic model successfully predicted the reduced glutamine consumption fluxes under high lactate culture conditions, along with a decrease in the conversion of glutamine to AKG. Consequently, the model also predicted slightly lower fluxes through key TCA cycle reactions such as α-ketoglutarate dehydrogenase, succinate dehydrogenase, malate dehydrogenase, fumarase, and citrate synthase.

Table 2 lists the predictions of biomass-specific uptake and production rates for critical extracellular metabolites at 12 and 36-h. The table also includes the average flux between 12 and 36-h, as determined by the Extracellular Time-Course Analysis (ETA) software (Murphy & Young, 2013), for comparison. The general mass balance equation, constructed by ETA, which describes the dynamics in the concentration of the *i*-th extracellular metabolite under batch growth conditions, is given by

$$\frac{ds_i(t)}{dt} = r_i X(t),$$

where $s_i(t)$ represents the concentration of the *i*-th metabolite at time *t*, r_i is the specific rate of metabolite consumption or production, and $X(t)$ stands for cell density at time *t*. This equation assumes no degradation of metabolites. Notice that ETA results are based on the assumption of metabolic steady-state, meaning that the consumption or production rate r_i of any *i*-th metabolite remains constant and it is not influenced by the changes in extracellular or intracellular concentrations. This assumption explains why most flux estimations using the ETA approach for 12–36-h fall within the range of the model predictions at 12 and 36-h.

Under conditions of limited substrate availability, there are significant changes in consumption rates, as exemplified by glucose in LGLL and LGHL cultures, as well as pyruvate in all four conditions. Unlike averaging approaches (e.g., ETA model), the proposed metabolic kinetic model effectively captures these essential dynamic behaviors. This capability holds promise for facilitating future research on the end-to-end cell culture process optimal control to improve high-quality iPSC production. Additionally, as stirred

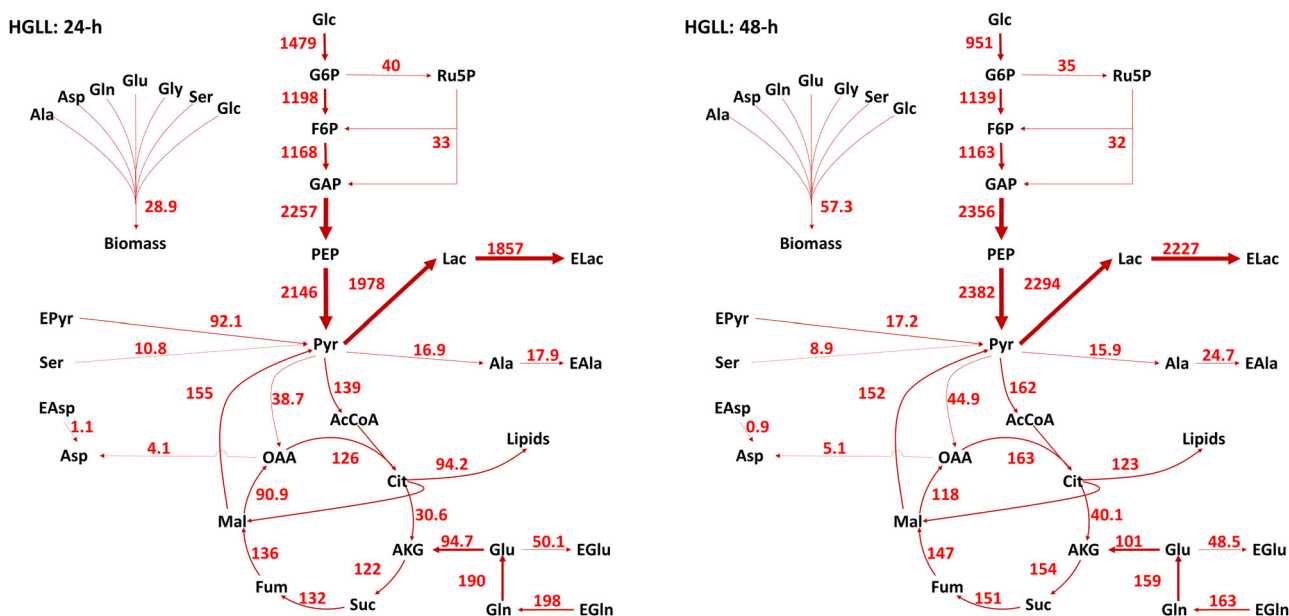


FIGURE 7 Metabolic flux maps for K3 iPSC for the high glucose and low lactate cultures at 24–48-h. Predicted fluxes are given in $\text{nmol}/10^6$ cells \cdot h. The line thicknesses represent the relative fluxes. iPSC, induced pluripotent stem cells.

TABLE 2 Dynamic model prediction for biomass-specific uptake and production rates for key extracellular metabolite ($\text{nmol}/10^6$ cells \cdot h).

Metabolite	HGHL ($\text{nmol}/10^6$ cells \cdot h)			LGHL ($\text{nmol}/10^6$ cells \cdot h)		
	12-h	36-h	12–36-h (ETA)	12-h	36-h	12–36-h (ETA)
Glucose	-1910	-1132	-1051	-1664	-826	-994
Lactate	1410	2145	2108	1400	2096	2000
Pyruvate	-109	-58.2	-67.7	-109	-60.2	-75.2
Glutamate	35.4	53.3	36.2	35.5	54.4	32.4
Glutamine	-221	-180	-132	-224	-178	-147
Metabolite	HGHL ($\text{nmol}/10^6$ cells \cdot h)			LGHL ($\text{nmol}/10^6$ cells \cdot h)		
	12-h	36-h	12–36-h (ETA)	12-h	36-h	12–36-h (ETA)
Glucose	-880	-773	-874	-763	-628	-860
Lactate	1332	1602	1694	1314	1388	1651
Pyruvate	-71.2	-53.4	-39	-71.9	-53.3	-36.5
Glutamate	31.1	49.2	28.3	31.6	49.8	29.4
Glutamine	-206	-161	-107	-202	-160	-120

Note: The fluxes obtained by Extracellular Time-Course Analysis (ETA) for 12–36-h are calculated averages from measurements (Odenwelder et al., 2021), while the 12 and 36-h fluxes predicted by the developed metabolic kinetic model are calculated for that specific time point. Negative values represent consumption rates and positive values represent production rates.

suspension cultures become a common choice for large-scale iPSC manufacturing (Borys et al., 2020; Meng et al., 2017), this study can also contribute to the understanding of cell behavior within aggregates, as the well-established pattern involves LGHL concentrations at the aggregate center (Kinney et al., 2011).

By modeling the regulatory mechanisms outlined in Section 3.3, the results presented in Table 2 are consistent with observations reported in existing studies (Costa Leite et al., 2007;

Ghorbaniaghdam et al., 2014, 2013, 2014; Glacken et al., 1988; Halestrap, 2012; Hassell et al., 1991; Huckabee, 1956; Ivarsson et al., 2015; Mulukutla et al., 2012). The ability of the proposed model to accurately predict cell dynamic behavior and response under varying environmental conditions reaffirms its reliability and underscores its potential to enhance the optimization and control of iPSC culture processes. Specifically, the model indicates that the consumption rate of glucose increases with higher extracellular glucose

concentrations (e.g., HGLL vs. LGLL and HGHL vs. LGHL), while it decreases with higher extracellular lactate concentrations (e.g., HGLL vs. HGHL and LGLL vs. LGHL). These trends can be attributed to regulatory mechanism **R1** as described in eq (7). Regarding lactate, the model reveals that the net production rate is lower when a certain amount of lactate exists in the cultural environment (e.g., HGLL vs. HGHL and LGLL vs. LGHL). In the case of pyruvate, under high lactate culture conditions, more favorable lactate transport kinetics of MCTs result in decreased pyruvate consumption (e.g., HGLL vs. HGHL and LGLL vs. LGHL). These observations are associated with regulatory mechanism **R6** as explained in eq (12). Furthermore, the presence of lactate dampens the conversion of glutamine to glutamate. Consequently, under high lactate culture conditions, the consumption rate of glutamine and the production rate of glutamate decrease (e.g., HGLL vs. HGHL and LGLL vs. LGHL). These behaviors are linked to regulatory mechanisms **R2** in eq (8) and **R7** in eq (13).

5 | CONCLUSIONS

In this paper, a metabolic kinetic model is described that characterizes the time-varying dynamics and regulatory mechanisms of the iPSC cultures. This model detailed central carbon metabolism, including glycolysis, TCA cycle, PPP, anaplerosis, and key amino acid metabolism. The iPSC metabolic regulatory network was calibrated using extracellular metabolite concentrations and intracellular isotopic data for multiple tracers (i.e., [1,2-¹³C₂] glucose and [U-¹³C₅] glutamine tracers). These time-course measurements were collected at multiple time points for the different culture conditions. The validation results demonstrate that the developed metabolic kinetic model can provide a reliable prediction on iPSC metabolic response to changes in extracellular glucose and lactate levels.

This model holds substantial potential for advancing the understanding of complex intracellular regulatory mechanisms within iPSC cultures. Furthermore, it empowers continuous monitoring and precise control of cell cultures, particularly advantageous in the realm of large-scale manufacturing. In summary, the proposed mechanistic model holds the potential to facilitate the optimization and control of iPSC cultures, potentially even at large scales, ensuring the survival, productivity, and quality of iPSC-derived cell products.

AUTHOR CONTRIBUTIONS

Keqi Wang: Conceptualization, methodology, investigation, coding, software, visualization, and writing—original draft. **Wei Xie:** Conceptualization, methodology, resources, supervision, and writing—review and editing. **Sarah W. Harcum:** Acquisition of data, visualization, interpretation, supervision, and writing—review and editing.

ACKNOWLEDGMENTS

The authors acknowledge the funding support from the National Institute of Standards and Technology (Grants 70NANB17H002 and

70NANB21H086) to Dr. Wei Xie and the National Science Foundation (Grant OIA-1736123 and EEC-2100442) to Sarah W. Harcum. Drs. Xie and Harcum are the co-corresponding authors.

DATA AVAILABILITY STATEMENT

The data that support the findings of this study are available from the corresponding author upon reasonable request.

ORCID

Wei Xie  <http://orcid.org/0000-0001-9563-4927>

Sarah W. Harcum  <http://orcid.org/0000-0001-9417-0489>

REFERENCES

- Ahn, W. S., & Antoniewicz, M. R. (2011). Metabolic flux analysis of CHO cells at growth and non-growth phases using isotopic tracers and mass spectrometry. *Metabolic Engineering*, 13(5), 598–609.
- Ahn, W. S., & Antoniewicz, M. R. (2013). Parallel labeling experiments with [1, 2-¹³C] glucose and [U-¹³C] glutamine provide new insights into CHO cell metabolism. *Metabolic engineering*, 15, 34–47.
- Antoniewicz, M. R. (2015). Methods and advances in metabolic flux analysis: a mini-review. *Journal of Industrial Microbiology and Biotechnology*, 42(3), 317–325.
- Antoniewicz, M. R. (2018). A guide to ¹³C metabolic flux analysis for the cancer biologist. *Experimental Molecular Medicine*, 50(4), 1–13.
- Antoniewicz, M. R. (2021). A guide to metabolic flux analysis in metabolic engineering: Methods, tools and applications. *Metabolic Engineering*, 63, 2–12.
- Antoniewicz, M. R., Kelleher, J. K., & Stephanopoulos, G. (2007). Elementary metabolite units (EMU): a novel framework for modeling isotopic distributions. *Metabolic Engineering*, 9(1), 68–86.
- Borys, B. S., So, T., Colter, J., Dang, T., Roberts, E. L., Revay, T., Larjani, L., Krawetz, R., Lewis, I., Argiropoulos, B., (2020). Optimized serial expansion of human induced pluripotent stem cells using low-density inoculation to generate clinically relevant quantities in vertical-wheel bioreactors. *Stem Cells Translational Medicine*, 9(9), 1036–1052.
- Chang, A., Jeske, L., Ulbrich, S., Hofmann, J., Koblit, J., Schomburg, I., Neumann-Schaal, M., Jahn, D., & Schomburg, D. (2021). BRENDA, the ELIXIR core data resource in 2021: new developments and updates. *Nucleic Acids Research*, 49(D1), D498–D508.
- CostaLeite, T., DaSilva, D., GuimarãesCoelho, R., Zancan, P., & Sola-Penna, M. (2007). Lactate favours the dissociation of skeletal muscle 6-phosphofructo-1-kinase tetramers down-regulating the enzyme and muscle glycolysis. *Biochemical Journal*, 408(1), 123–130.
- Dong, W., Moon, S. J., Kelleher, J. K., & Stephanopoulos, G. (2019). Dissecting mammalian cell metabolism through 13c-and 2h-isotope tracing: interpretations at the molecular and systems levels. *Industrial & Engineering Chemistry Research*, 59(6), 2593–2610.
- Draoui, N., & Feron, O. (2011). Lactate shuttles at a glance: from physiological paradigms to anti-cancer treatments. *Disease Models & Mechanisms*, 4(6), 727–732.
- Dressel, R. (2011). Effects of histocompatibility and host immune responses on the tumorigenicity of pluripotent stem cells. In *Seminars in Immunopathology*, (Vol. 33, pp. 573). Springer.
- Fiorenza, S., Ritchie, D. S., Ramsey, S. D., Turtle, C. J., & Roth, J. A. (2020). Value and affordability of CAR T-cell therapy in the United States. *Bone Marrow Transplantation*, 55(9), 1706–1715.
- Ghorbaniaghdam, A., Chen, J., Henry, O., & Jolicoeur, M. (2014). Analyzing clonal variation of monoclonal antibody-producing CHO cell lines using an in silico metabolomic platform. *PLoS One*, 9(3), e90832.
- Ghorbaniaghdam, A., Henry, O., & Jolicoeur, M. (2013). A kinetic-metabolic model based on cell energetic state: study of CHO cell

- behavior under Na-butyrate stimulation. *Bioprocess and Biosystems Engineering*, 36, 469–487.
- Ghorbaniaghdam, A., Henry, O., & Jolicoeur, M. (2014). An in-silico study of the regulation of CHO cells glycolysis. *Journal of Theoretical Biology*, 357, 112–122.
- Glacken, M., Adema, E., & Sinskey, A. (1988). Mathematical descriptions of hybridoma culture kinetics: I. initial metabolic rates. *Biotechnology and Bioengineering*, 32(4), 491–506.
- Halestrap, A. P. (2012). The monocarboxylate transporter family-structure and functional characterization. *IUBMB Life*, 64(1), 1–9.
- Hanna, E., Rémuzat, C., Auquier, P., & Toumi, M. (2016). Advanced therapy medicinal products: current and future perspectives. *Journal of Market Access & Health Policy*, 4(1), 31036.
- Hassell, T., Gleave, S., & Butler, M. (1991). Growth inhibition in animal cell culture: The effect of lactate and ammonia. *Applied Biochemistry and Biotechnology*, 301, 29–41.
- Huckabee, W. E. (1956). Control of concentration gradients of pyruvate and lactate across cell membranes in blood. *Journal of Applied Physiology*, 9(2), 163–170.
- Ivarsson, M., Noh, H., Morbidelli, M., & Soos, M. (2015). Insights into pH-induced metabolic switch by flux balance analysis. *Biotechnology Progress*, 31(2), 347–357.
- Jazmin, L. J., & Young, J. D. (2013). Isotopically nonstationary ¹³C metabolic flux analysis. *Systems Metabolic Engineering: Methods and Protocols*, 985, 367–390.
- Kinney, M. A., Sargent, C. Y., & McDevitt, T. C. (2011). The multi-parametric effects of hydrodynamic environments on stem cell culture. *Tissue Engineering Part B: Reviews*, 17(4), 249–262.
- Kyriakopoulos, S., Ang, K. S., Lakshmanan, M., Huang, Z., Yoon, S., Gunawan, R., & Lee, D.-Y. (2018). Kinetic modeling of mammalian cell culture bioprocessing: The quest to advance biomanufacturing. *Biotechnology Journal*, 13(3), 1700229.
- Leighty, R. W., & Antoniewicz, M. R. (2011). Dynamic metabolic flux analysis (DMFA): A framework for determining fluxes at metabolic non-steady state. *Metabolic Engineering*, 13(6), 745–755.
- McLachlan, G. J. (2005). *Discriminant analysis and statistical pattern recognition*. John Wiley & Sons.
- Meng, G., Liu, S., Poon, A., & Rancourt, D. E. (2017). Optimizing human induced pluripotent stem cell expansion in stirred-suspension culture. *Stem Cells and Development*, 26(24), 1804–1817.
- Mulukutla, B. C., Gramer, M., & Hu, W.-S. (2012). On metabolic shift to lactate consumption in fed-batch culture of mammalian cells. *Metabolic Engineering*, 14(2), 138–149.
- Murphy, T. A., & Young, J. D. (2013). ETA: robust software for determination of cell specific rates from extracellular time courses. *Biotechnology and Bioengineering*, 110(6), 1748–1758.
- Nelson, D. L., Lehninger, A. L., & Cox, M. M. (2008). *Lehninger Principles of Biochemistry*. Macmillan.
- Niklas, J., & Heinzle, E. (2012). Metabolic flux analysis in systems biology of mammalian cells. *Genomics and Systems Biology of Mammalian Cell Culture*, 127, 109–132.
- Nolan, R. P., & Lee, K. (2011). Dynamic model of CHO cell metabolism. *Metabolic Engineering*, 13(1), 108–124.
- Odenwelder, D. C., Lu, X., & Harcum, S. W. (2021). Induced pluripotent stem cells can utilize lactate as a metabolic substrate to support proliferation. *Biotechnology Progress*, 37(2), e3090.
- Quek, L.-E., Dietmair, S., Krömer, J. O., & Nielsen, L. K. (2010). Metabolic flux analysis in mammalian cell culture. *Metabolic Engineering*, 12(2), 161–171.
- Refaeilzadeh, P., Tang, L., & Liu, H. (2009). Cross-validation. *Encyclopedia of Database Systems*, 6, 532–538.
- Rivera-Ordaz, A., Peli, V., Manzini, P., Barilani, M., & Lazzari, L. (2021). Critical analysis of cGMP Large-Scale expansion process in bioreactors of human induced pluripotent Stem Cells in the Framework of Quality by Design. *BioDrugs*, 35(6), 693–714.
- Sengupta, N., Rose, S. T., & Morgan, J. A. (2011). Metabolic flux analysis of CHO cell metabolism in the late non-growth phase. *Biotechnology and Bioengineering*, 108(1), 82–92.
- Stephanopoulos, G., Aristidou, A. A., & Nielsen, J. (1998). *Metabolic engineering: Principles and methodologies*.
- Templeton, N., Dean, J., Reddy, P., & Young, J. D. (2013). Peak antibody production is associated with increased oxidative metabolism in an industrially relevant fed-batch CHO cell culture. *Biotechnology and Bioengineering*, 110(7), 2013–2024.
- Wang, L. L.-W., Janes, M. E., Kumbhojkar, N., Kapate, N., Clegg, J. R., Prakash, S., Heavey, M. K., Zhao, Z., Anselmo, A. C., & Mitragotri, S. (2021). Cell therapies in the clinic. *Bioengineering & Translational Medicine*, 6(2), e10214.
- Wiechert, W., Möllney, M., Petersen, S., & De Graaf, A. A. (2001). A universal framework for ¹³C metabolic flux analysis. *Metabolic Engineering*, 3(3), 265–283.
- Young, J. D., Walther, J. L., Antoniewicz, M. R., Yoo, H., & Stephanopoulos, G. (2008). An elementary metabolite unit (emu) based method of isotopically nonstationary flux analysis. *Biotechnology and Bioengineering*, 99(3), 686–699.

How to cite this article: Wang, K., Xie, W., & Harcum, S. W. (2024). Metabolic regulatory network kinetic modeling with multiple isotopic tracers for iPSCs. *Biotechnology and Bioengineering*, 121, 1335–1353. <https://doi.org/10.1002/bit.28609>

APPENDIX A: APPENDIX: TABLE

The following tables summarize detailed information about the constructed induced pluripotent stem cells (iPSCs) metabolic network and developed kinetic model.

1. The iPSC metabolic network contains the major reactions for glycolysis, the tricarboxylic acid (TCA) cycle, anaplerosis, pentose phosphate pathway (PPP), and amino acid metabolism; see the specific reactions in Table A1. The reactions of PPP are collapsed into two: Oxidative phase/branch and Non-oxidative phase/branch (i.e., No. 9 & 10 reactions).
2. The iPSC metabolic flux rate regulation biokinetic model is summarized in Table A2. The Michaelis-Menten (MM) model is used to characterize how key activators and inhibitors influence regulatory mechanisms in each reaction.
3. The descriptions of the metabolites, considered in the developed metabolic kinetic model, are listed in Table A3.

4. For the developed metabolic kinetic model, the descriptions of the enzymes with Enzyme Commission Number (EC-No.) are provided in Table A4. They are associated with metabolic flux reaction rates.

TABLE A1 Reactions of the metabolic network.

No.	Pathway
Glycolysis	
1	Glc(abcdef) → G6P(abcdef)
2	G6P(abcdef) → F6P(abcdef)
3	F6P(abcdef) → GAP(cba) + GAP (def)
4	GAP(abc) → PEP(abc)
5	PEP(abc) → Pyr(abc)
6	Pyr(abc) ↔ Lac(abc)
7	EPyr(abc) → Pyr(abc)
8	Lac(abc) ↔ ELac(abc)
PPP	
9	G6P(abcdef) → Ru5P(bcdef) + CO ₂ (a)
10	Ru5P(abcde) + Ru5P(fghij) + Ru5P(klmno) → F6P(fgahij) + F6P(klbcde) + GAP(mno)
TCA	
11	Pyr(abc) → AcCoA(bc) + CO ₂ (a)
12	AcCoA(ab) + OAA(cdef) → Cit(fedbac)
13	Cit(abcdef) ↔ AKG(abcde) + CO ₂ (f)
14	AKG(abcde) → Suc(bcde) + CO ₂ (a)
15	Suc(abcd) → Fum(abcd)
16	Fum(abcd) ↔ Mal(abcd)
17	Mal(abcd) ↔ OAA(abcd)
Anaplerosis and Amino Acid	
18	Mal(abcd) → Pyr(abc) + CO ₂ (d)
19	Pyr(abc) + CO ₂ (d) → OAA(abcd)
20	Gln(abcde) ↔ Glu(abcde) + NH ₄
21	Glu(abcde) ↔ AKG(abcde) + NH ₄
22	Glu(abcde) + Pyr(fgh) ↔ AKG(abcde) + Ala(fgh)
23	Ala(abc) → EAla(abc)
24	Glu(abcde) → EGlu(abcde)
25	EGln(abcde) → Gln(abcde)
26	Ser(abc) → Pyr(abc) + NH ₄
27	Asp(fghi) + AKG(abcde) ↔ Glu(abcde) + OAA(fghi) + NH ₄
28	EAsp(abcd) → Asp(abcd)
29	Cit(abcdef) → Mal(fcba) + Lipids
Biomass	
30	0.19 Ala + 0.11 Asp + 0.1 Gln + 0.12 Glu + 0.17 Gly + 0.14 Ser + 0.16 Glc → Biomass

TABLE A2 Biokinetic equations of the metabolites fluxes (1–30) of the model.

No.	Pathway
Glycolysis	
1	$v(HK) = v_{max,HK} \times \frac{Glc}{K_{m,Glc} + Glc} \times \frac{K_i,G6P}{K_i,G6P + G6P} \times \frac{K_i,LactoHK}{K_i,LactoHK + Lac}$
2	$v(PGI) = v_{max,PGI} \times \frac{G6P}{K_{m,G6P} + G6P}$
3	$v(PFK/ALD) = v_{max,PFK/ALD} \times \frac{F6P}{K_{m,F6P} + F6P}$
4	$v(PGK) = v_{max,PGK} \times \frac{GAP}{K_{m,GAP} + GAP}$
5	$v(PK) = v_{max,PK} \times \frac{PEP}{K_{m,PEP} \times (1 + \frac{K_a,F6P}{F6P}) + PEP}$
6f	$vLDHf = v_{max,fLDH} \times \frac{Pyr}{K_{m,Pyr} + Pyr}$
6r	$v(LDHr) = v_{max,rLDH} \times \frac{Lac}{K_{m,Lac} + Lac} \times \frac{K_i,Pyr}{K_i,Pyr + Pyr}$
7	$v(PyrT) = v_{max,PyrT} \times \frac{EPyr}{K_{m,EPyr} + EPyr} \times \frac{K_i,LactoPyr}{K_i,LactoPyr + Lac}$
8f	$v(LacTf) = v_{max,fLacT} \times \frac{Lac}{K_{m,Lac} + Lac}$
8r	$v(LacTr) = v_{max,rLacT} \times \frac{ELac}{K_{m,ELac} + ELac}$
PPP	
9	$v(OP) = v_{max,OP} \times \frac{G6P}{K_{m,G6P} + G6P}$
10	$v(NOP) = v_{max,NOP} \times \frac{Ru5P}{K_{m,Ru5P} + Ru5P}$
TCA	
11	$v(PDH) = v_{max,PDH} \times \frac{Pyr}{K_{m,Pyr} + Pyr}$
12	$v(CS) = v_{max,CS} \times \frac{AcCoA}{K_{m,AcCoA} + AcCoA} \times \frac{OAA}{K_{m,OAA} + OAA}$
13f	$v(CITS/ISODf) = v_{max,fCITS/ISOD} \times \frac{Cit}{K_{m,Cit} + Cit}$
13r	$v(CITS/ISODr) = v_{max,rCITS/ISOD} \times \frac{AKG}{K_{m,AKG} + AKG}$
14	$v(AKGDH) = v_{max,AKGDH} \times \frac{AKG}{K_{m,AKG} + AKG}$
15	$v(SDH) = v_{max,SDH} \times \frac{Suc}{K_{m,Suc} + Suc}$
16f	$v(FUMf) = v_{max,fFUM} \times \frac{Fum}{K_{m,Fum} + Fum}$
16r	$v(FUMr) = v_{max,rFUM} \times \frac{Mal}{K_{m,Mal} + Mal}$
17f	$v(MDHf) = v_{max,fMDH} \times \frac{Mal}{K_{m,Mal} + Mal}$
17r	$v(MD Hr) = v_{max,rMDH} \times \frac{OAA}{K_{m,OAA} + OAA}$
Anaplerosis and Amino Acid	
18	$v(ME) = v_{max,ME} \times \frac{Mal}{K_{m,Mal} + Mal}$
19	$v(PC) = v_{max,PC} \times \frac{Pyr}{K_{m,Pyr} + Pyr}$
20f	$v(GLNSf) = v_{max,fGLNS} \times \frac{Gln}{K_{m,Gln} + Gln} \times \frac{K_i,LactoGLNS}{K_i,LactoGLNS + Lac}$
20r	$v(GLNSr) = v_{max,rGLNS} \times \frac{Glu}{K_{m,Glu} + Glu} \times \frac{NH_4}{K_{m,NH_4} + NH_4}$
21f	$v(GLDHf) = v_{max,fGLDH} \times \frac{Glu}{K_{m,Glu} + Glu}$

(Continues)

TABLE A2 (Continued)

No.	Pathway
21r	$v(\text{GLDHR}) = v_{\max, \text{rGLDHR}} \times \frac{\text{AKG}}{K_{\text{m,AKG}} + \text{AKG}} \times \frac{\text{NH}_4}{K_{\text{m,NH}_4} + \text{NH}_4}$
22f	$v(\text{AlaTAF}) = v_{\max, \text{fAlaTA}} \times \frac{\text{Glu}}{K_{\text{m,GLU}} + \text{Glu}} \times \frac{\text{Pyr}}{K_{\text{m,Pyr}} + \text{Pyr}}$
22r	$v(\text{AlaTAr}) = v_{\max, \text{rAlaTA}} \times \frac{\text{Ala}}{K_{\text{m,Ala}} + \text{Ala}} \times \frac{\text{AKG}}{K_{\text{m,AKG}} + \text{AKG}} \times \left(1 + \frac{K_{\text{a,Gln}}}{\text{Gln}}\right)$
23	$v(\text{AlaT}) = v_{\max, \text{AlaT}} \times \frac{\text{Ala}}{K_{\text{m,Ala}} + \text{Ala}}$
24	$v(\text{GluT}) = v_{\max, \text{GluT}} \times \frac{\text{Glu}}{K_{\text{m,Glu}} + \text{Glu}}$
25	$v(\text{GlnT}) = v_{\max, \text{GlnT}} \times \frac{\text{EGln}}{K_{\text{m,EGln}} + \text{EGln}} \times \frac{K_{\text{i,GLN}}}{K_{\text{i,GLN}} + \text{GLN}}$
26	$v(\text{SAL}) = v_{\max, \text{SAL}} \times \frac{\text{Ser}}{K_{\text{m,Ser}} + \text{Ser}}$
27f	$v(\text{ASTAf}) = v_{\max, \text{fASTA}} \times \frac{\text{Asp}}{K_{\text{m,ASP}} + \text{Asp}} \times \frac{\text{AKG}}{K_{\text{m,AKG}} + \text{AKG}}$
27r	$v(\text{ASTAr}) = v_{\max, \text{rASTA}} \times \frac{\text{Glu}}{K_{\text{m,Glu}} + \text{Glu}} \times \frac{\text{OAA}}{K_{\text{m,OAA}} + \text{OAA}} \times \frac{\text{NH}_4}{K_{\text{m,NH}_4} + \text{NH}_4}$
28	$v(\text{AspT}) = v_{\max, \text{AspT}} \times \frac{\text{EAsp}}{K_{\text{m,EAsp}} + \text{EAsp}}$
29	$v(\text{ACL}) = v_{\max, \text{ACL}} \times \frac{\text{Cit}}{K_{\text{m,Cit}} + \text{Cit}}$
	Biomass
30	$v(\text{growth}) = v_{\max, \text{growth}} \times \frac{\text{Gln}}{K_{\text{m,Gln}} + \text{Gln}} \times \frac{\text{Glc}}{K_{\text{m,Glc}} + \text{Glc}} \times \frac{\text{Glu}}{K_{\text{m,Glu}} + \text{Glu}}$ $\times \frac{\text{Ala}}{K_{\text{m,Ala}} + \text{Ala}} \times \frac{\text{Asp}}{K_{\text{m,Asp}} + \text{Asp}} \times \frac{\text{Ser}}{K_{\text{m,Ser}} + \text{Ser}} \times \frac{\text{Gly}}{K_{\text{m,Gly}} + \text{Gly}}$

TABLE A3 Description of the metabolite.

Component	Description	Component	Description
ACCoA	Acetyl-CoenzymeA	ALA	Alanine
AKG	α -Ketoglutarate	ASP	Aspartate
CIT	Citrate	LAC	Lactate
CO2	Intracellular Carbonoxygen	GLN	Glutamine
F6P	Fructose 6-Phosphate	EGLY	Extracellular Glycine
G6P	Glucose 6-Phosphate	SER	Extracellular Serine
GAP	Glyceraldehyde 3-Phosphate	GLC	Extracellular Glucose
GLU	Glutamate	EGLN	Extracellular Glutamine
GLY	Glycine	EGLU	Extracellular Glutamate
MAL	Malate	EPYR	Extracellular Pyruvate
OAA	Oxaloacetate	EASP	Extracellular Aspartate
PEP	Phosphoenolpyruvate	EALA	Extracellular Alanine
FUM	Fumarate	ELAC	Extracellular Lactate
Ru5P	Ribulose 5-Phosphate	NH4	Extracellular Ammonia
SUC	Succinate	LIPID	Lipid
PYR	Pyruvate	Bio	Biomass

TABLE A4 Description of the enzyme.

Abbreviation	Description	EC-No.
HK	Hexokinase	2.7.1.1
PGL	Phosphoglucose Isomerase	5.3.1.9
PFK/ALD	Phosphofructokinase/Aldolase	2.7.1.11/4.1.2.13
PGK	Phosphoglycerate Kinase	2.7.2.3
PK	Pyruvate Kinase	2.7.1.40
OP	Oxidative Phase of PPP	
NOP	Non-oxidative Phase of PPP	
PyrT	Membrane Transport of Pyruvate	
SAL	Membrane Transport of Serine	
LDH	Lactate Dehydrogenase	1.1.1.27
AlaTA	Alanine Transaminase	2.6.1.2
PC	Pyruvate Carboxylase	6.4.1.1
PDH	Pyruvate Dehydrogenase	1.2.4.1
CS	Citrate (Si)-Synthase	2.3.3.1
CITS/ISOD	Aconitase/Isocitrate Dehydrogenase	4.2.1.3/1.1.1.41
GLDH	Glutamate Dehydrogenase	1.4.1.2
GluT	Membrane Transport of Glutamate	
GLNS	Glutamine Synthetase	6.3.1.2
AKGDH	α -ketoglutarate Dehydrogenase	1.2.1.105
SDH	Succinate Dehydrogenase	1.3.5.1
MDH	Malate Dehydrigenase	1.1.1.37
ME	Malic Enzyme	1.1.1.40
ASTA	Aspartate Aminotransferase	2.6.1.1
ACL	ATP citrate synthase	2.3.3.8
FUM	Fumarase	4.2.1.2

APPENDIX B: APPENDIX: CELL CHARACTERISTIC PREDICTIONS

Figures B1–B3 depict the model's predictions for iPSC cultures in three scenarios: high glucose and high lactate (HGHL), low glucose and low lactate (LGLL), and low glucose and high lactate cultures (LGHL). Predictions are based on training the model using data collected over various time intervals.

APPENDIX C: APPENDIX: CELL CHARACTERISTIC ACROSS CULTURE CONDITION PREDICTIONS

Figures C1–C3 depict prediction results across various initial conditions, including high glucose and high lactate (HGHL), LGLL, and LGHL. The model's fitting is based on data from the remaining three cases.

APPENDIX D: APPENDIX: METABOLIC FLUX MAPS

Figure D1–D3 depict the metabolic flux maps for iPSC culture at 24–48-h respectively under the initial conditions, including HGHL, LGLL, and LGHL.

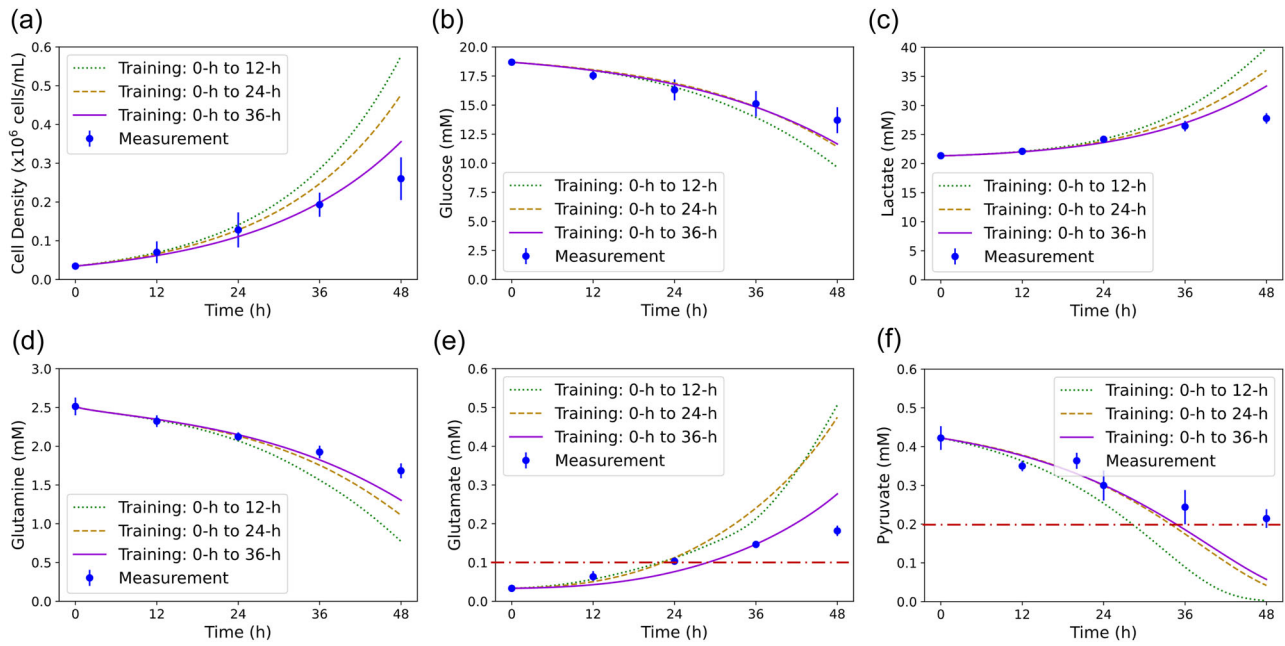


FIGURE B1 Dynamic model trained with different time intervals—Cell characteristic predictions for high glucose and high lactate cultures. (a) Cell density, (b) Glucose, (c) Lactate, (d) Glutamine, (e) Glutamate, and (f) Pyruvate. Times 0–12-h (green dotted line); Times 0–24-h (brown dashed line); and Times 0-h to 36-h (purple solid line). The detection limit of the Cedex Bioanalyzer is shown as the red dash-dot line.

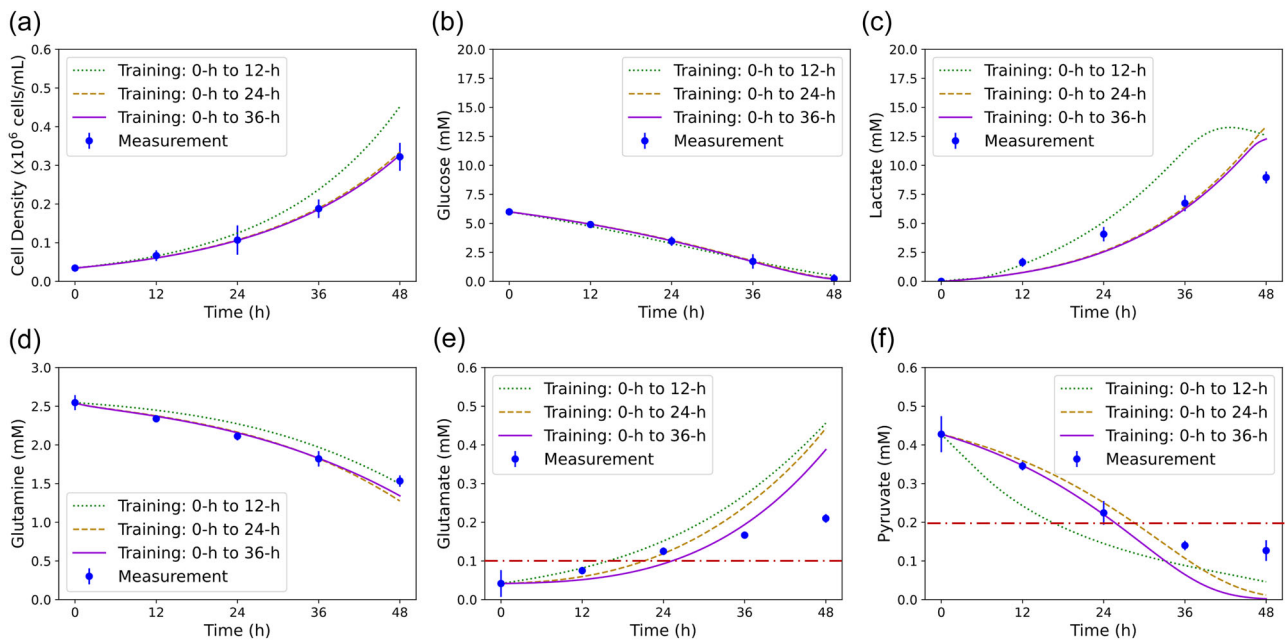


FIGURE B2 Dynamic model trained with different time intervals—Cell characteristic predictions for low glucose and low lactate cultures. (a) Cell density, (b) Glucose, (c) Lactate, (d) Glutamine, (e) Glutamate, and (f) Pyruvate. Times 0–12-h (green dotted line); Times 0–24-h (brown dashed line); and Times 0–36-h (purple solid line). The detection limit of the Cedex Bioanalyzer is shown as the red dash-dot line.

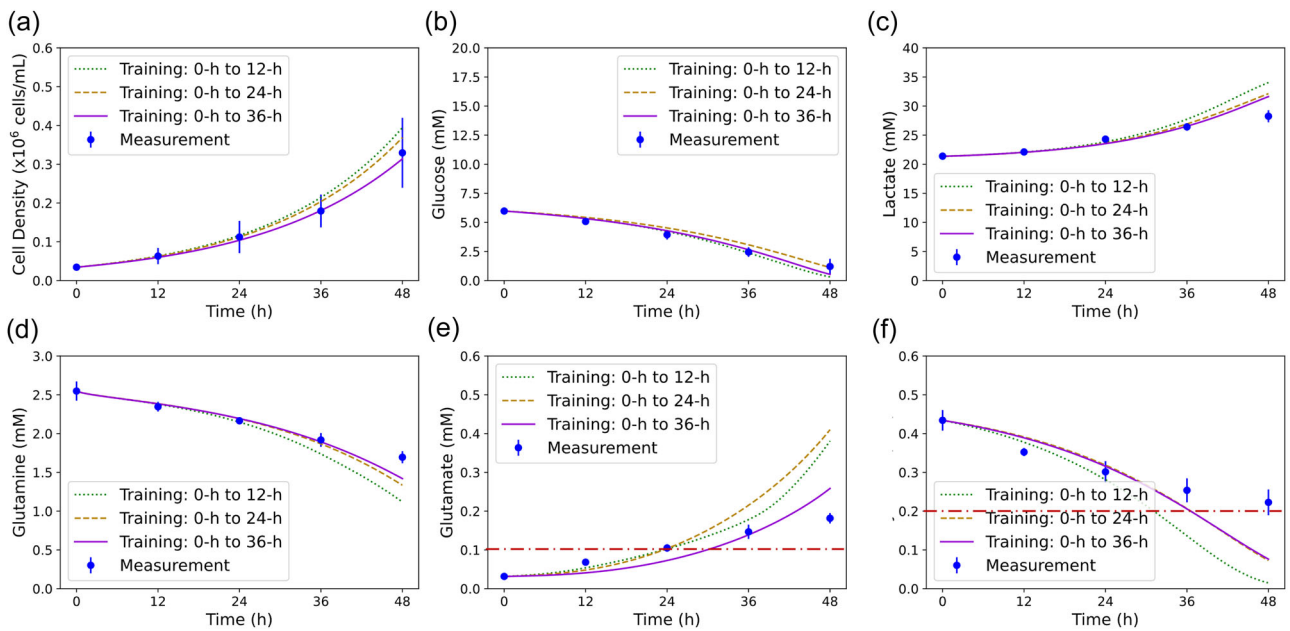


FIGURE B3 Dynamic model trained with different time intervals - Cell characteristic predictions for low glucose and high lactate cultures. (a) Cell density, (b) Glucose, (c) Lactate, (d) Glutamine, (e) Glutamate, and (f) Pyruvate. Times 0–12-h (green dotted line); Times 0–24-h (brown dashed line); and Times 0–36-h (purple solid line). The detection limit of the Cedex Bioanalyzer is shown as the red dash-dot line.

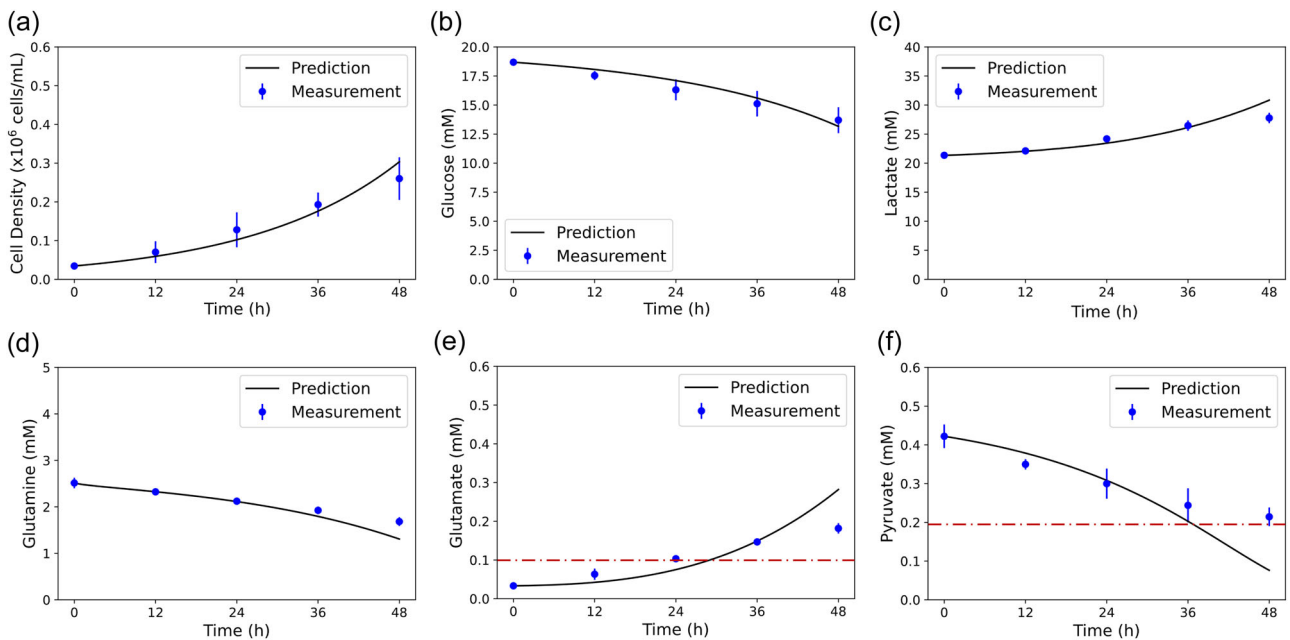


FIGURE C1 Dynamic model trained with three other data sets with varied initial glucose and lactate concentrations for cell characteristic predictions in high glucose and high lactate cultures. (a) Cell density, (b) Glucose, (c) Lactate, (d) Glutamine, (e) Glutamate, and (f) Pyruvate. The detection limit of the Cedex Bioanalyzer is shown as the red dash-dot line.

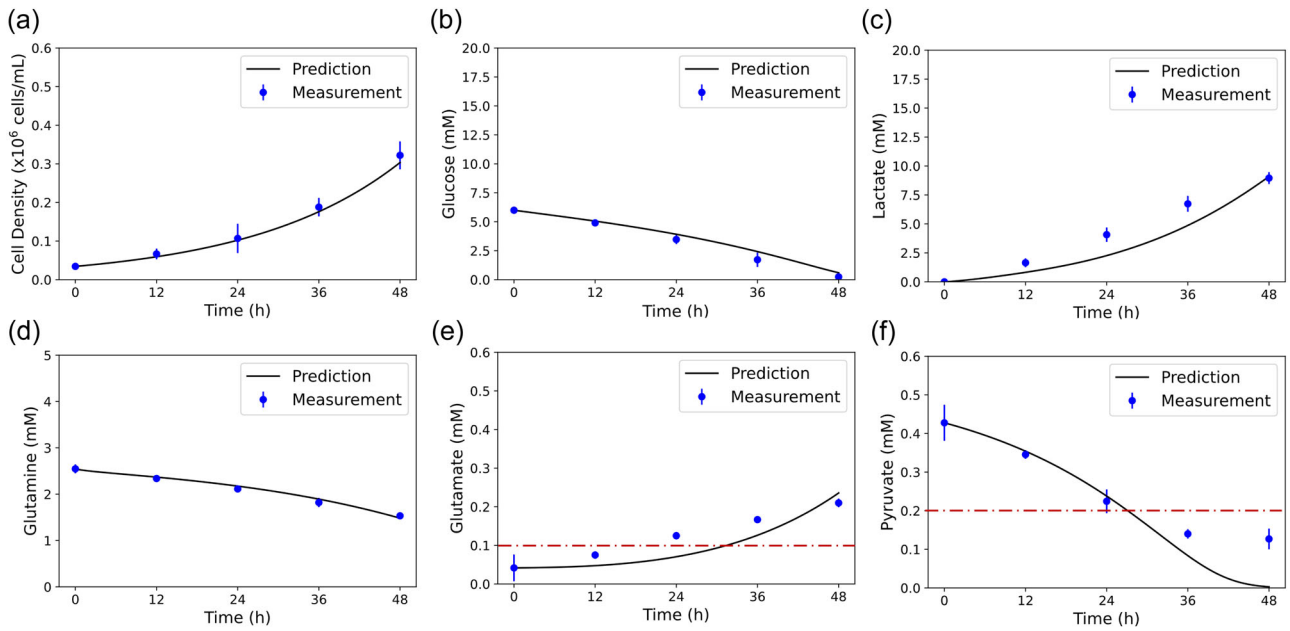


FIGURE C2 Dynamic model trained with three other data sets with varied initial glucose and lactate concentrations for cell characteristic predictions in low glucose and low lactate cultures. (a) Cell density, (b) Glucose, (c) Lactate, (d) Glutamine, (e) Glutamate, and (f) Pyruvate. The detection limit of the Cedex Bioanalyzer is shown as the red dash-dot line.

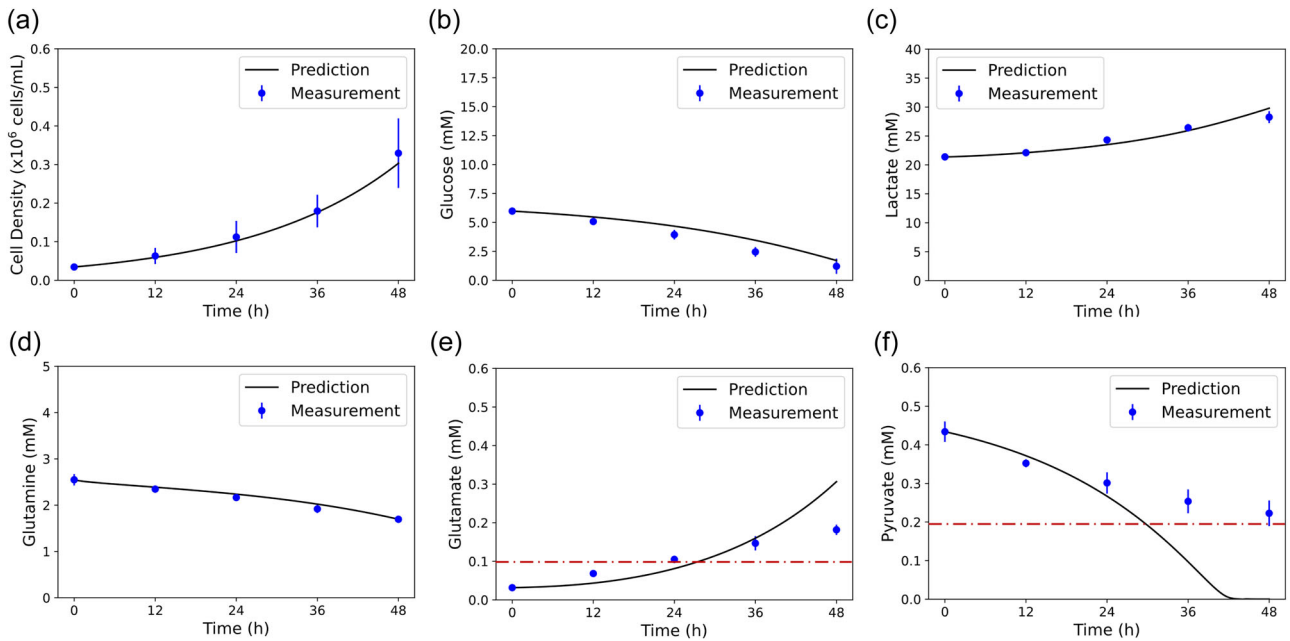


FIGURE C3 Dynamic model trained with three other data sets with varied initial glucose and lactate concentrations for cell characteristic predictions in low glucose and high lactate cultures. (a) Cell density, (b) Glucose, (c) Lactate, (d) Glutamine, (e) Glutamate, and (f) Pyruvate. The detection limit of the Cedex Bioanalyzer is shown as the red dash-dot line.

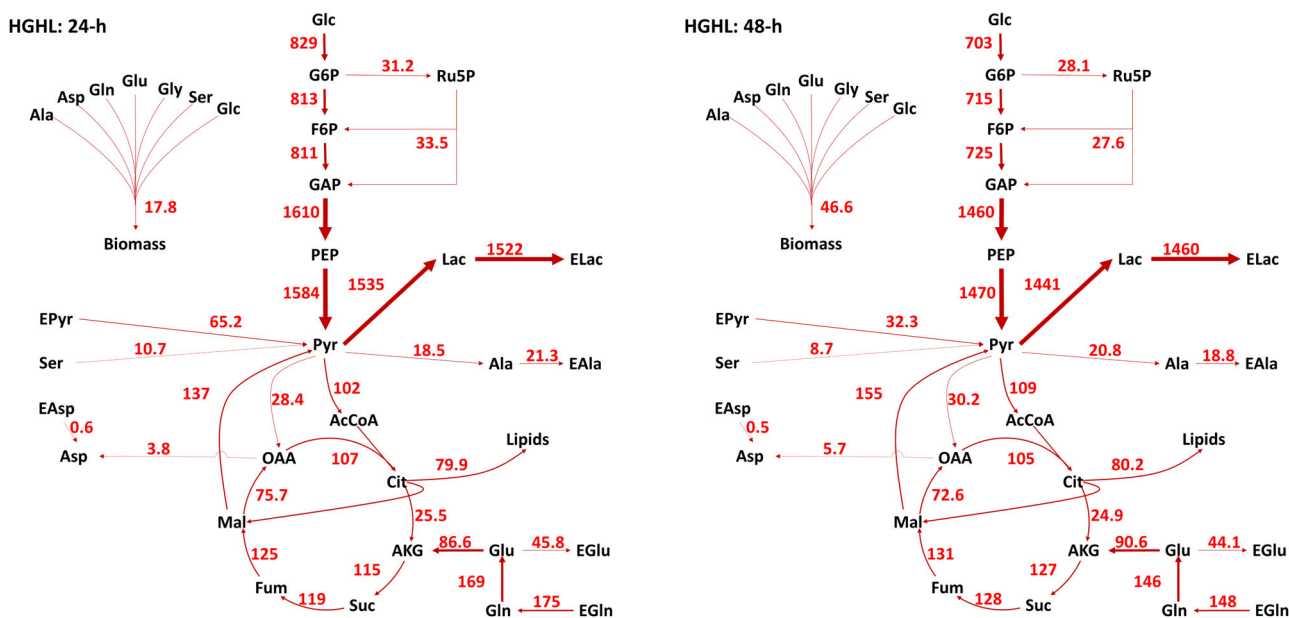


FIGURE D1 Metabolic flux maps for K3 iPSC for the high glucose and high lactate cultures at 24–48-h. Predicted fluxes are given in nmol/ 10^6 cells·h. The line thicknesses represent the relative fluxes. iPSC, induced pluripotent stem cells.

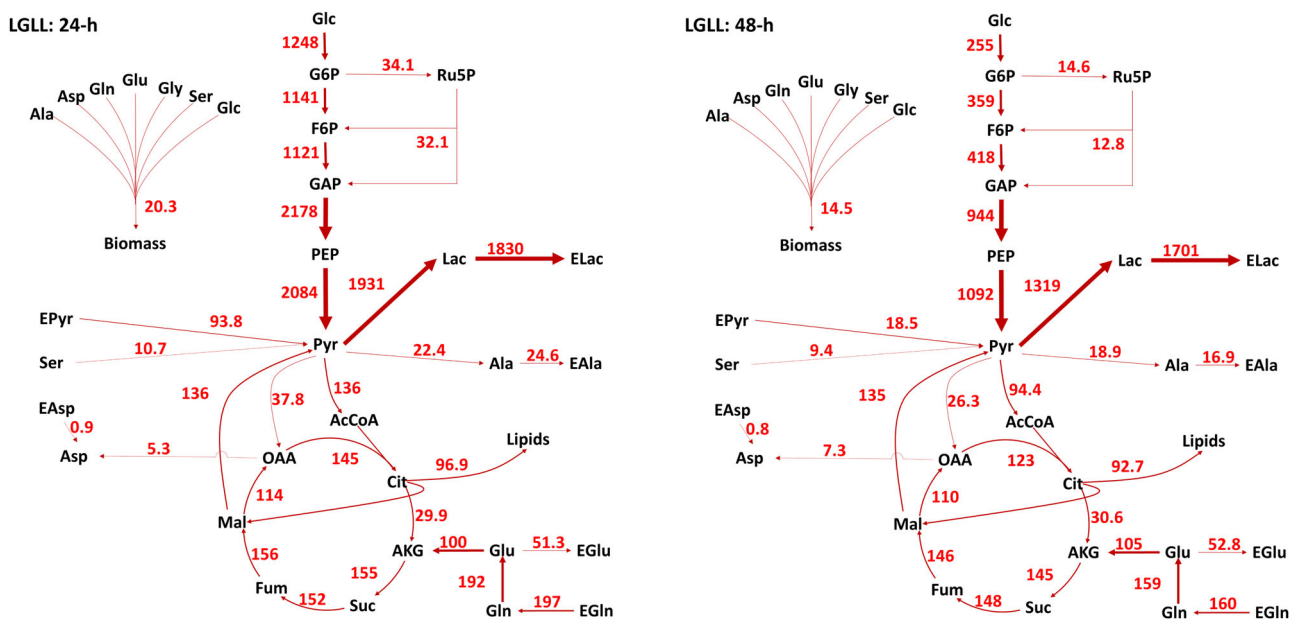


FIGURE D2 Metabolic flux maps for K3 iPSC for the low glucose and low lactate cultures at 24–48-h. Predicted fluxes are given in nmol/ 10^6 cells·h. The line thicknesses represent the relative fluxes. iPSC, induced pluripotent stem cells.

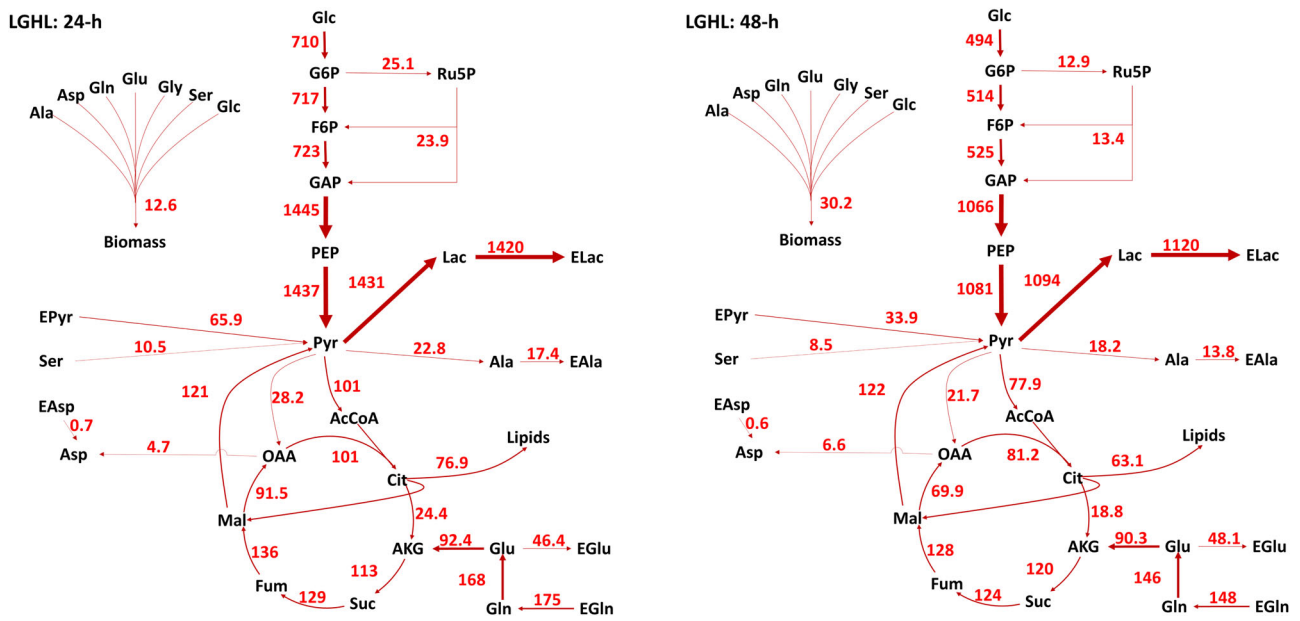


FIGURE D3 Metabolic flux maps for K3 iPSC for the low glucose and high lactate cultures at 24–8-h. Predicted fluxes are given in nmol/10⁶ cells·h. The line thicknesses represent the relative fluxes. iPSC, induced pluripotent stem cells.